Using Shelf-Edge Transport Composition and Sensitivity Experiments to Understand Processes Driving Sea Level on the Northwest European Shelf

A. Wise[1] , F. M. Calafat[1] , C. W. Hughes[2] , S. Jevrejeva[1] , C. A. Katsman[3] , J. Oelsmann[4] , C. Piecuch[5] , J. Polton[1] , and K. Richter[6]

[1]National Oceanography Centre, Liverpool, UK, [2]University of Liverpool, Liverpool, UK, [3]Delft University of Technology, Delft, The Netherlands, [4]Technical University of Munich, Munich, Germany, [5]Woods Hole Oceanographic Institution, Woods Hole, MA, USA, [6]NORCE Norwegian Research Centre AS, Bergen, Norway

Abstract Variability in ocean currents, temperature and salinity drive dynamic sea level (DSL) variability on the Northwest European Shelf (NWES). It is dominated by mass variations, with steric signals relatively small. A mechanistic explanation of how ocean dynamics relates to the mass component of NWES sea level variability is required. We use regional ocean model experiments to isolate sources of variability and then investigate the effect on monthly to-interannual DSL variability together with the simulated momentum budgets along the shelfbreak. Regional (local) wind and non-regional (remote) forcing are important on the NWES. For the local wind forcing, the net mass flux onto the shelf, which drives a shelf-mean mode of DSL variability, results from a combination of surface Ekman, bottom Ekman and geostrophic flows and explains 73% of the variance in transport across the shelf-edge. The geostrophic flow is closely related to wind stress with a flow about half that of surface Ekman transport but in the opposite direction. For the remotely forced mass-flux across the shelf-edge, the geostrophic component explains 62% of the variance and bottom friction plays an important indirect role. The remotely forced variability, while relatively spatially uniform, is more important for explaining DSL variance over the western NWES. This mode of variability is sensitive to signals propagating northward via a thin strip of the southern boundary near the Portuguese coast, consistent with coastal trapped wave signals. It also appears to drive steric height in the Bay of Biscay, which is related to DSL on the shelf.

Plain Language Summary Changes in sea level on the North West European Shelf (NWES) that result from changes in ocean currents, temperature and salinity have many sources. The shelf-mean sea level changes as the volume of water on the shelf changes. Variations in the amount of water flowing onto the NWES is, consequently, a link between ocean currents and coastal sea level. We run experiments in a regional ocean model that isolate sources of variability. We then investigate the effect on both sea level and the processes that determine ocean currents. Winds redistribute water onto the shelf through Ekman transport. We find that winds also drive water across the shelf-edge indirectly, and find the volume of water transported across the shelf-edge in this way is approximately half that due to wind driven Ekman transport, but in the opposite direction. Non-regional forcing, associated with non-local winds, modifies the pressure gradient along the shelfbreak and results in changes in the amount of water on the NWES. This remote forcing is associated with density variations in the adjacent ocean. Both the coastal and oceanic sea levels are sensitive to oceanic changes occurring at lower latitudes and which travel northward along the shelfedge.

1. Introduction

On interannual-to-decadal timescales there is a mode of sea-level variability around the UK coastline that is correlated with a larger mode of North Atlantic eastern boundary (NAEB) variability (Hogarth et al., 2020). This larger-scale mode extends along the eastern boundary from the coastlines of North Africa into the Arctic basin. Hogarth et al. (2020) drew on tide gauge analysis and results from Calafat et al. (2012) and Fukumori et al. (2015) to suggest that wind-driven boundary signals could be the driving mechanism. In this study we use perturbation experiments and monthly mean momentum budget diagnostics from an ocean circulation model simulating 2006–2015 to quantify the relative roles of local and remote forcing mechanisms on dynamic sea level (DSL) on the North West European Shelf (NWES) on monthly to-interannual timescales. We use "local" in reference to processes within the NWES model domain and "remote" in reference to variability originating at the lateral boundary conditions. A mechanistic understanding is important when quantifying the effect of DSL drivers to

Validation: A. Wise
Visualization: A. Wise
Writing – original draft: A. Wise
Writing – review & editing: A. Wise, F. M. Calafat, C. W. Hughes, S. Jevrejeva, C. A. Katsman, J. Oelsmann, C. Piecuch, J. Polton, K. Richter

reduce uncertainty in the interpretation of cause and effect, this is particularly true when isolating relatively small magnitude or low frequency variability, for example, due to changes in the large scale ocean circulation. For example, the authors of the Royal Netherlands Meteorological Institute National Climate Scenarios 2023 (van Dorland et al., 2023) consider models by the quality of DSL simulation once wind effects have been statistically removed. This is because over the sub-decadal selection period the intrinsic variability of the winds can have a large impact on sea level trends. A consequence of improved understanding is a greater confidence in our ability to simulate future climate scenarios.

A number of studies have suggested that local wind forcing is an important source of DSL variability on the NWES. Chafik et al. (2017) found that coherent changes in deseasonalized monthly sea level project onto a combination of the positive phase North Atlantic Oscillation (NAO+) and positive phase Scandinavia (SCAN+) atmospheric teleconnection patterns. They argued that these atmospheric patterns combined to create atmospheric pressure gradients across the continental boundary that resulted in wind stress along the continental slope. They concluded that this led to a pile-up of water along European coasts via the surface Ekman transport mechanism. Hermans et al. (2022) also concluded that changes in regional wind stress were the dominant driver of changes in coastal DSL on seasonal timescales via Ekman transport redistribution. Similarly, by association with configurations of the eddy-driven jet stream, Mangini et al. (2021) argue that the resulting wind-driven Ekman transport is an important mechanism explaining sea level patterns on the NWES. The effects of wind forcing via Ekman transport have been shown to be particularly important on intra- and interannual timescales along the southern and eastern coasts of the North Sea (Dangendorf et al., 2014; Hermans et al., 2020).

While the sea-level response to wind stress via Ekman transport is relatively local and rapid (for monthly periods, the equilibrium response is established approximately instantaneously) there is a more subtle response to wind-stress forcing that can produce a non-local (remote) response. For example, on monthly to-interannual timescales, Fukumori et al. (2015) showed that across the Arctic-North African region, winds over the continental slope in the southern portion of the region produced a remote sea-level and bottom-pressure response further northward. They argued that barotropic coastal trapped waves were responsible for the coherence. Furthermore, Sturges and Douglas (2011) and Calafat et al. (2012) argued that coastal trapped waves are a dominant source of coastal sea-level variability along the eastern North Atlantic boundary at lower frequencies. They showed that interannual-to-decadal sea-level variability on the eastern boundary of the North Atlantic is highly correlated with along-shore wind stress that is integrated northward from close to the equator. Unlike Ekman transport, this indicates a response to the cumulative along-shore wind stress, propagated poleward by coastal trapped waves.

Local and remote along-shore winds are also an important factor when considering the effect of large-scale ocean variability. Winds may be important as a mechanism for the redistribution of deep ocean water masses across the continental slope (Chafik et al., 2019; Marsh et al., 2017). When local winds and remotely generated variability covary, however, it can be difficult to isolate the deep ocean contribution and interpret causality in any associated sea-level variability. For example, Piecuch et al. (2019) demonstrated that the Atlantic Meridional Overturning Circulation (AMOC) and US east coast DSL shared a common driver in the large scale atmospheric variability that could result in erroneously concluding that the AMOC drove coastal DSL variability when in fact local winds and atmospheric pressure were the causal drivers. The relative importance and mechanisms involved in deep ocean effects on coastal DSL have been studied in a number of publications in relation to the western boundary of the North Atlantic (e.g., Hong et al., 2000; Lin et al., 2022; Piecuch et al., 2019; Wang et al., 2022; Wise, Polton, et al., 2020; Woodworth et al., 2014, and others). Far less attention has been directed at eastern boundaries, however. To the extent that it has, there is no consensus on the mechanism(s) by which deep ocean variability might drive coastal sea level on the NWES, or whether winds are an important part of this mechanism.

Woodworth et al. (2010) used air pressure and coastal sea level data commencing in the middle of the eighteenth century to show a possible relationship between air pressure in the middle of the subtropical gyre, redistribution of water, and annual mean sea level at Brest. This built upon Miller and Douglas's (2007) suggestion that eastern boundary coastal sea level responds to wind forced gyre-scale ocean adjustments. Despite this, Calafat et al. (2012) did not find a strong association between eastern boundary coastal sea level and simulated subtropical gyre strength on interannual-to-decadal timescales. In the context of seas adjacent to the eastern boundary, Dangendorf et al. (2014) and Frederikse et al. (2016) have shown that a coherent mode of sea level variability on the NWES is correlated with the adjacent deep ocean steric height (notably the region around the Bay of Biscay). Dangendorf et al. (2021) further demonstrate that interannual-to-decadal sea level in the North Sea can be

reconstructed from steric heights in the adjacent deep ocean (again notably around the Bay of Biscay). They refer to the open ocean region as a source of variability, implying that open ocean steric variability drives DSL variability on the shelf, however they do not explore the processes.

Two mechanisms involving wind forcing have been suggested for the NWES. Chafik et al. (2019) noted that along-shore wind stress and North Atlantic subpolar gyre strength and spatial extent are both associated with sea level on the NWES. They argued that off-shelf steric anomalies influence DSL on the shelf via cross-shelf heat fluxes due to wind-driven Ekman transport. Alternatively, Frederikse et al. (2016) hypothesized that the correlation with the open ocean could result from the radiation of Rossby waves away from the continental slope and toward the open ocean. This would occur when wind-generated coastal trapped waves, which propagate along the boundary, also radiate long Rossby waves into the deep ocean. This could result in covariation between DSL on the shelf and deep ocean steric anomalies.

These differences of interpretation underscore the difficulty of inferring causation from correlation. Conducting specific experiments using models can provide a more definitive causal attribution. Tinker et al. (2020) used annual means from a regional NEMO model of the NWES that downscaled a present-day control simulation of a climate model to run experiments where either atmospheric or lateral boundaries were controlled for. This allowed them to assess the effect of local atmospheric and remote forcing on interannual-to-decadal variability. They found the local and remote sources of variability combined linearly, and that the remote forcing resulted in a uniform change in sea level on the shelf. The local atmospheric forcing resulted in spatial DSL variability with a larger mean amplitude than the remote forcing. With similar experiments, Hermans et al. (2020) used annual means from a ROMS regional model of the NWES and reanalysis data to partition atmospheric forcing into individual components for interannual variability. They found the inverse barometer effect, local winds and the cumulative effect of local along-shore winds to be key drivers of the local DSL interannual variability. They also found that both the western and southern lateral boundaries generated interannual DSL variability on the NWES.

A component missing from the literature is a mechanistic and quantitative assessment of the remotely and locally forced processes driving DSL, relative to one another. For example, what is the importance of Ekman transport relative to locally and remotely forced geostrophic transports? Are non-linear transports important? In this study we seek to begin filling this gap for monthly to-interannual variability. We follow the approach of Tinker et al. (2020) and Hermans et al. (2020) in conducting perturbation experiments but focus on higher frequency variability (monthly means) using a NEMO based NWES regional model with reanalysis forcing. To these studies we also add an analysis of the momentum equations around the shelfedge, which enables us to isolate both the dynamic processes and the DSL variability that results from different forcing. We use this to develop a leading order relationship between DSL on the shelf and cross-shelfedge circulation over the period 2006–2015. We note that the relative importance of different forcing terms can change over time and a longer set of experiments would be required to determine the scale of any such change.

We structure the remainder of the paper as follows. In Section 2 we describe the data, model and experiments that we use and conduct. In Section 3 we present our results, starting with a reference model-observation comparison of the modes of variability on the NWES (Section 3.1). We then use the perturbation experiments to separate remote and local sources of DSL variability (Section 3.2). In Section 3.3 a framework is developed that relates remotely forced shelf edge ocean dynamics with near-coast DSL and in Section 3.4 we show that a large proportion of this remote forcing originates close to the Portuguese coast at the southern boundary of our domain.

2. Data and Experiments

The ocean model used for our analysis is the NEMO 7 km horizontal resolution Atlantic Margin Model (AMM7) configuration described and used by Wise et al. (2021). The NEMO configuration and source files are available from the repository (Wise, Polton, & Harle, 2024). The model covers the NWES and adjacent Atlantic Ocean, which extends to over 5,000 m offshore of Portugal, see Figure 1, and has 51 vertical levels. It is forced using hourly ERA5 surface forcing (Hersbach et al., 2018) and the Global Seasonal Forecast System version 5 data set (MacLachlan et al., 2015) for daily lateral boundaries. Flather (1976) conditions are used for the depth-mean velocities at the boundaries, flow relaxation for the tracers and zero gradient for the 3d velocities. The daily river discharge forcing is constructed from the climatology of daily discharge data from the Global River Discharge Database (Vörösmarty et al., 2000) combined with an updated version of the river data used in Lenhart et al. (2010) and data prepared by the Center for Ecology and Hydrology, as used by Young and Holt (2007).
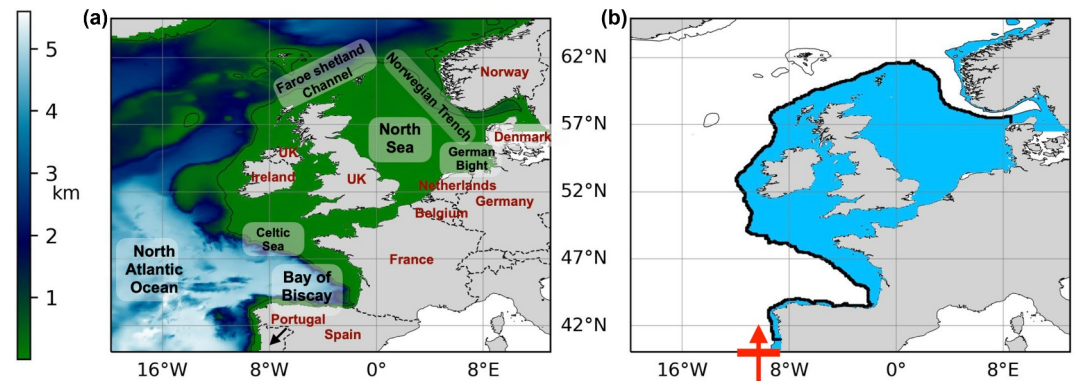
Figure 1. Model domain with (a) the bathymetry and (b) the blue region indicating the North West European Shelf where the bathymetry is ≤200 m. In (b) The thick black line indicates a section of 200 m isobath and two transects at the ends that connect with the coast. The red line indicates a section of the lateral boundary that is set to the 10 years mean value in the *bdy_block_ctw* experiment.

Fifteen tidal constituents are also applied at the open lateral boundaries. This configuration of the AMM7 model builds upon a previous configuration evaluated in O'Dea et al. (2017) with an updated multi-envelope (Bruciaferri et al., 2018) vertical coordinate system designed to reduce pressure gradient errors in terrain-following vertical coordinate systems (Wise et al., 2021) (configuration MEs_r10_r07) and is maintained for research and operational purposes. From the model we output monthly means over the period 2006–2015.

For model comparison with observations we use tide gauges as well as satellite altimetry. We use 31 tide gauges around the NWES selected to ensure a relatively consistent spatial distribution around the shelf. Data is monthly, covering the period 2006–2015, and is from the Permanent Service for Mean Sea Level (2022) (Holgate et al., 2013). Gaps in the record are filled with a linear interpolation; for the sites selected there is a maximum of 1 missing record in each site's entire record with the exception of the Les Sables-d'Olonne site, which has an anomalous period of 5 consecutive months without data. We also compare the model sea surface height against absolute dynamic topography (ADT) derived from altimetry observations. For this we use the gridded L4 sea surface height EUR regional 0.125° resolution product from the Copernicus Marine Service (CMEMS, 2023a). This product applies corrections to remove high frequency variability induced by the atmospheric forcing and aliased by the altimeters measurement, and removes the inverse barometer effect due to low frequency (>20 days) atmospheric pressure forcing. The product also applies a correction for tides and long wavelength errors. We resample the daily ADT fields into monthly means and regrid onto the AMM7 spatial grid. For analysis extending beyond the European region we use the sea level anomaly (SLA) monthly mean fields from the 0.25° resolution Copernicus Marine Service product (CMEMS, 2023b).

Unless otherwise stated data have been linearly detrended and deseasonalized by removing the 10-year average for each month. Gradients in atmospheric pressure can be used to force hydrostatic model dynamics via the momentum equations by introducing an inverse barometer sea surface height, η_{ib}, to the pressure gradient term. Model experiments are run without this option enabled and tide gauges are corrected using $\eta_{ib} = -(p_a - p_0)/(g\rho_0)$, where p_a is the monthly mean atmospheric pressure, $p_0 = 1{,}010$ mbar is a constant reference pressure (in principle this would be the time varying global mean atmospheric pressure, although this varies by a relatively small degree; mainly an approximate 0.5 mbar amplitude annual cycle, see (Hughes et al., 2012)), $g = 9.8$ m s^{-2} is the gravitational constant and $\rho_0 = 1{,}026$ kg m^{-3} is a reference density. Here p_a is taken from the ERA5 reanalysis data set used to force the model. Note that η_{ib} is a relatively large source of variability in sea level on the European Shelf (Hermans et al., 2020) and other regions (e.g., Piecuch & Ponte, 2015). On monthly time scales the effect is mostly isostatic (Piecuch et al., 2022). The monthly mean model sea surface height when run with constant atmospheric pressure in the momentum equations is consistent with that found when run with varying atmospheric pressure, if an inverse barometer correction is applied to the output. Hence for our investigation removing this effect serves to help investigate the remaining drivers of variability.

The ocean model was used to run a set of experiments with the aim of quantifying how sea level and momentum dynamics change under different forcing scenarios. For a given experiment the influence of specific forcing

Table 1
Experiments Conducted

Experiment name	Wind	Surface (non-wind)	Lateral boundary	Lateral boundary off-shore of Portugal	Evaporation, precipitation, rivers	Tides
ref	✓	✓	✓	✓	✓	✓
nowind		✓	✓	✓	✓	✓
bdy			✓	✓		
bdy_block_ctw			✓			
nobdy	✓	✓			✓	✓

Note. The first column gives the experiment name and the remaining columns indicate the boundary forcing used in each experiment, where a ✓ denotes that variability in the forcing was preserved. Where there is no ✓, it means that the specific forcing is set to its time-mean value for the particular experiment. Here "Surface" refers to all forcing (excluding wind) supplied to the model at the boundary with the atmosphere.

variables on ocean state variability is removed by using the 2006–2015 time mean for those specific forcing variables, similarly to the experiments of Tinker et al. (2020) and Hermans et al. (2020).

We conducted the following five experiments, which are summarized in Table 1.

- (*ref*) is a realistic reference simulation with all forcing applied.
- (*nowind*) is the same as the reference, but without wind forcing variability (i.e., wind inputs are replaced by their time-mean). This is used to investigate the sensitivity of dynamics to local wind forcing.
- (*bdy*) is forced only with variability in the lateral boundary conditions (all other forcings are set to their respective time-mean values). This allows us to isolate the effects of remote forcing.
- (*bdy_block_ctw*) is the same as *bdy*, except that time-mean forcings are imposed at the section of lateral boundary extending across the shelf and continental slope from the coast of Portugal to a deep ocean point (see red line in Figure 1). This experiment is used to investigate the sensitivity of remotely forced variability to coastal trapped waves (CTW) entering from south of the domain.
- (*nobdy*) is the same as the reference simulation, but with lateral boundary conditions set to their time-mean values. This allows us to isolate the effects of local atmospheric and river forcing.

3. Results

3.1. Leading Modes of Variability in the Reference Run

Our approach in this study is to use the model to represent modes of variability that are coherent over large extents of the shelf and coast. We use Empirical Orthogonal Function (EOF) analysis (e.g., Hannachi et al., 2007) (based on the cross-covariance matrix) to identify the spatial and temporal projections of the modes, which we refer to as the EOF and Principle Component (PC), respectively.

Throughout the paper, where we compare time series, r is the correlation coefficient and s is the fraction of variance explained (expressed as a percentage) when one time series is used to explain another without any rescaling. This is defined by

$$s = \left[1 - \frac{\text{var}(a-b)}{\text{var}(a)} \right] 100\%,\tag{1}$$

where var $(\cdot)$ is the variance operator, and where we are assessing the skill of b to explain a. If optimal scaling is used by least-squares fitting, then $s = r^2$.

We perform the EOF analysis on the model DSL and satellite altimetry ADT across all grid points on the shelf, where the shelf is defined as model points where the bathymetry does not exceed 200 m (see region marked blue in Figure 1). Note, Figures S1-S3 in Supporting Information S1 of the supplementary information show that simulated monthly to-interannual DSL variability is a reasonable reconstruction of observed sea level at individual tide gauges around the NWES. The leading three modes of the EOF decomposition account for 83% of the variance in the observations. Figures 2a and 2c show the three leading PCs for the model and altimetry observations, where each have been divided by their standard deviations. The correlation coefficient between model and observation for
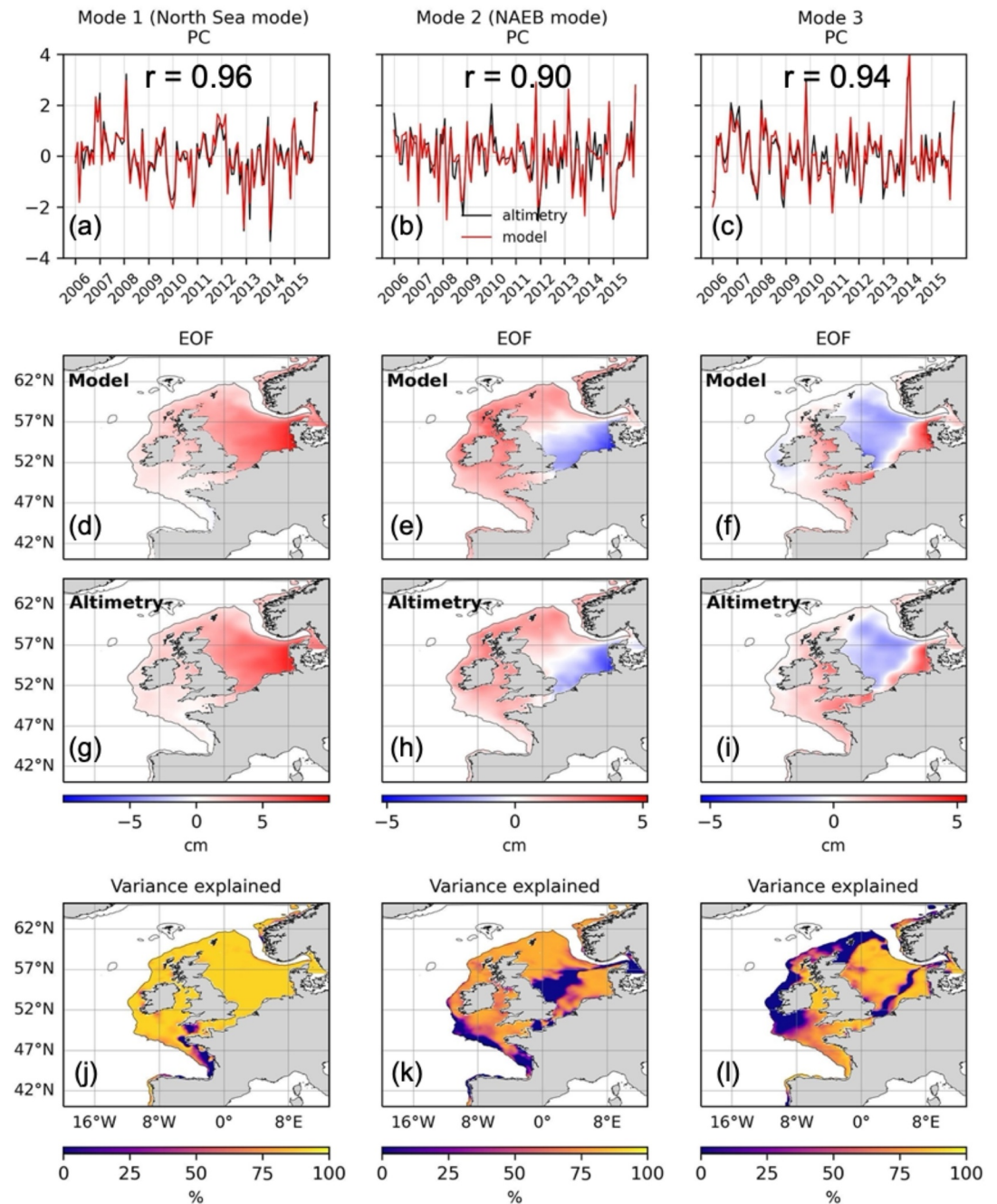
Figure 2. Empirical Orthogonal Function (EOF) modal decomposition comparing model reference dynamic sea level with altimetry derived absolute dynamic topography. EOF decomposition applied to all model grid points on the North West European Shelf (bathymetry ≤200). From left to right, columns 1–3 are the leading three modes. The first row compares the PCs (divided by standard deviation) with black lines for altimetry and red lines for model. The second row shows the model EOFs scaled by the Principle Component (PC) standard deviation. The third row shows the altimetry EOFs scaled by the PC standard deviation. The fourth row shows the percentage of variance in the observed mode explained by the simulated mode at each grid point using Equation 1.

each mode is $r = 0.96$, 0.90 and 0.94, respectively, demonstrating that the model represents the phase with a high degree of skill. The second and third rows in Figure 2 show the spatial structures as EOFs (scaled by the standard deviation) for the model (Figures 2c, 2e, and 2f) and observations (Figures 2g–2i), respectively. In each case the model closely represents the geographic distribution of the variability. The second and third rows of the first column show that mode one is largest in the North Sea, but extends around the UK and Ireland, as well as the

Norwegian shelf. This mode increases in magnitude in the southern North Sea and the coastlines of Germany, the Netherlands and Denmark. We refer to this as the North Sea mode. The second column EOFs in Figure 2 (Figures 2e and 2h) show in-phase variation along the entire western portion of the shelf with magnitudes of the same order. This extends to the northern portion of the shelf and across the Norwegian shelf. The southern North Sea varies in anti-phase with a magnitude of the same order. We refer to this mode as part of the NAEB mode, in anticipation of results showing that this mode is part of a much larger pattern of variability. The third mode EOFs shown in Figures 2f and 2i (third column) show a dipole in the North Sea between the region close to the German, Dutch and Danish coasts (German Bight) and the seas farther northward. The seas on the western portion of the shelf are out of phase with the majority of the North Sea such that the eastern and western coasts of Britain are in anti-phase. This spatial pattern closely resembles the change in winter- and summer-time seasonal DSL anomaly on the NWES under climate change scenarios shown by Hermans et al. (2022). They demonstrated that a strengthening of southwesterly winds produced the winter anomaly (in-phase with our Figures 2f and 2i), while northeasterly wind strengthening resulted in a phase reversal. This is consistent with what would be expected of wind-driven volume transport and this is a logical explanation for our mode 3, albeit on monthly timescales.

The fourth row in Figure 2 (Figures 2j–2l) shows the percentage of variance explained in the observations by the model at each grid point on the shelf using Equation 1. This gives a statistical measure of how the model represents the observations in terms of phase and amplitude at each grid point and for each mode. In all three cases the simulated modes explain over 80% of the variance in the observed modes at the majority of locations. There are two notable exceptions. Firstly, the shelf edge on the southwestern portion of the shelf in mode 2 has a simulated amplitude that is too large. Secondly, the northwestern portion of the shelf in mode 3 has a simulated amplitude that is out of phase with the observations. While the model's representation of the satellite derived leading modes of variance is not exact at each grid point, it is clear from the EOFs and PCs that the model captures the shelf-scale structure reasonably well. We can be confident that the simulated ocean dynamics driving DSL are sensible at the shelf-scale, which is our focus.

To confirm that the shelf-scale structures also occur at the coastline, we perform the same EOF analysis using tide-gauge observations. We take the model DSL at grid-cells closest to 31 tide-gauge sites and perform an EOF analysis over the time series at all sites. This is repeated for the observed sea level at each tide-gauge site. The first three modes combined account for 78% of the observed variability. Figures 3a and 3c show the three leading PCs for the model and observations, where each have been divided by their standard deviation. In each case the model closely represents the mode phase in the observations with correlation coefficients of r = 0.96, 0.87 and 0.90, respectively. The tide-gauge PC correlation coefficients with the equivalent altimetry PC are r = 0.88, 0.87 and 0.77, for modes 1–3, respectively. The high correlation indicates that variability at the coast varies in phase with the larger-scale spatial structures over the shelf.

The second and third rows in Figure 3 show the EOFs (scaled by the PC standard deviation) for the same three modes from the model (Figures 3d–3f) and observations (Figures 3g–3i), respectively. In each case the model closely represents the geographic distribution of the variability. The first (North Sea) mode has a uniform phase around the UK and North Sea and the largest amplitude (extreme >30 cm), along the coasts of Germany, the Netherlands and Denmark. The second (NAEB) mode has a uniform phase along the coastlines on the western side of the shelf, which is in anti-phase with the coastlines in the southern North Sea. The maximum amplitude is close to 15 cm. The third mode is in phase along the eastern coastline of Britain, where the largest amplitude is approximately 15 cm. The fourth row in Figure 3 (Figures 3j–3l) shows the variance explained at each site using Equation 1. The model represents the shelf-scale structure of variance in the observed coastal sea level modes with reasonable skill, with the east coast of the UK in mode 2 being the only clear exception.

The comparison has shown that the leading modes of shelf-scale variability have spatial structures that extend from the shelfedge to the coast. While the modeled modes may not be perfect representations of the observed variance at every tide gauge and grid point, the EOFs and PCs show that the model represents the shelf-scale variance reasonably. This gives confidence that the simulated dynamics driving DSL at the shelf-scale are sensible and suitable for analysis at such scales. Shelf-scale biases in ocean currents and temperature and salinity gradients should be apparent in the leading DSL modes, which are a reflection of how those variables affect water column volume. In addition, note that comparisons of the models simulated 2006–2015 temperature and salinity against EN4 profiles (Good et al., 2013), water mass properties in the Faroe-Shetland channel, and tidal harmonics have been performed previously in Wise et al. (2021).
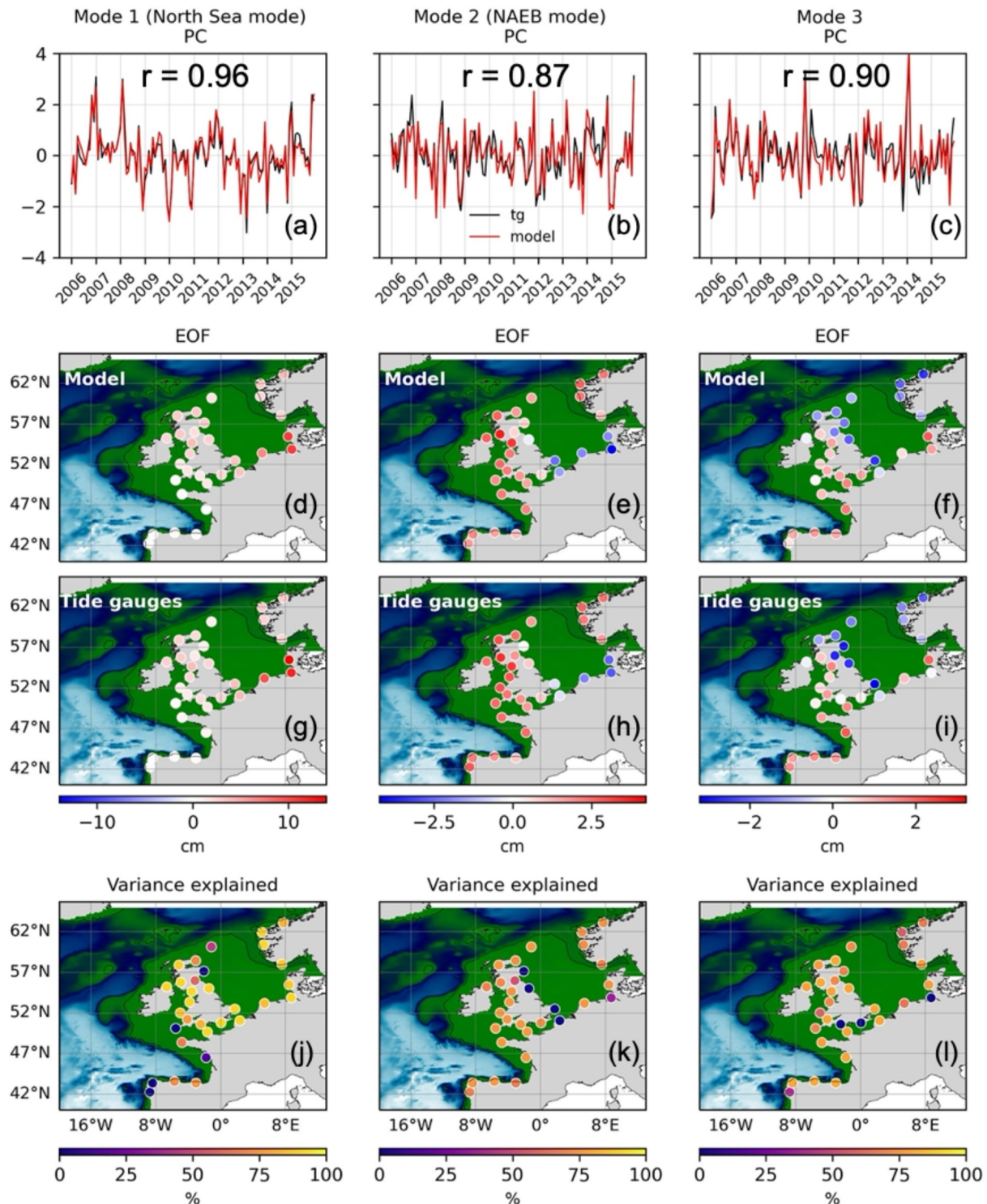
Figure 3. Empirical Orthogonal Function (EOF) decomposition comparing model reference dynamic sea level with tide gauge observations. EOF decomposition applied to all model grid points closest to each tide gauge. From left to right, columns 1–3 are the leading three modes. The first row compares the PCs (divided by the standard deviation) with black line for tide gauges and red lines for model. The second row shows the model EOFs scaled by the Principle Component (PC) standard deviation. The third row shows the tide gauge EOFs scaled by the PC standard deviation. The fourth row shows the percentage of variance in the observed mode explained by the simulated mode at each grid point using Equation 1. In (d)–(i) the bathymetry is shown using the colormap of Figure 1a.
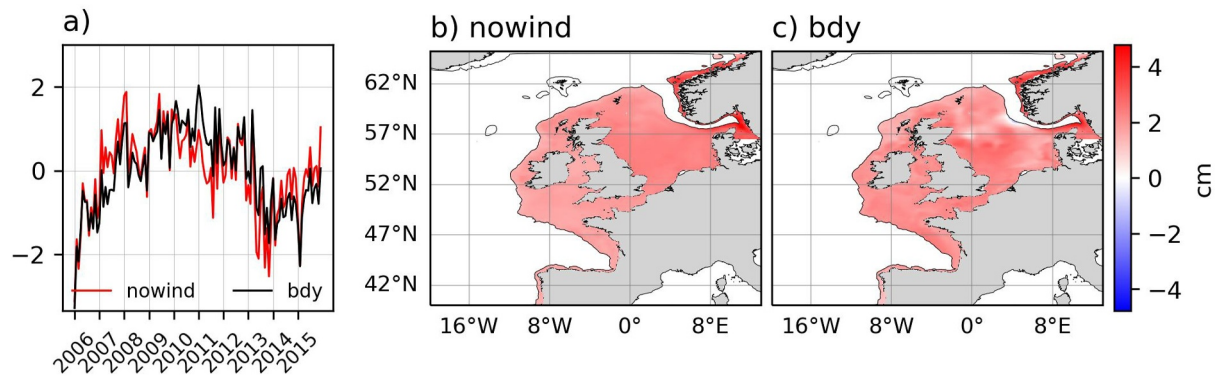
Figure 4. Comparison of the leading mode Principle Component (PC) and Empirical Orthogonal Function for dynamic sea level from the *nowind* and *bdy* experiments. Panel (a) shows the PC (divided by the standard deviation) for *nowind* and *bdy* (red, black, respectively). Panels (b) and (c) show the EOFs for the *nowind* and *bdy* experiments, respectively, each scaled by the associated PC standard deviation.

3.2. Remote and Local Modes of Variability

3.2.1. Local Wind Forcing

Tinker et al. (2020) decomposed NWES DSL variability into loading and redistribution terms and found atmospheric forcing to be principally responsible for the loading. By removing the local winds we find that there is an 82% reduction in shelf-average DSL variance, that is, changes in the total volume of water on the shelf (volume loading).

As in previous studies (e.g., Chafik et al., 2017; Dangendorf et al., 2014; Frederikse et al., 2016; Hermans et al., 2020; Wakelin et al., 2003), we also find local wind forcing is responsible for driving large shelf-scale spatial structures in DSL. For example, Figures 4a and 4b show the leading mode PC and EOF, respectively, for the *nowind* experiment. This leading mode of variability accounts for 79% of the total variance. The absence of spatial structure in the EOF compared to Figures 2d–2f demonstrates this point.

When DSL changes and the density of the water column is unchanged, then volume and mass change together. This can occur when winds pile water onto or across the shelf. Buoyancy fluxes can also modify DSL by changing the water column density resulting in expansion/contraction. Chafik et al. (2019) hypothesized that on interannual-to-decadal timescales the wind-driven DSL variability on the NWES can also be due to Ekman heat-fluxes transporting heat from the deep ocean onto the shelf. This heat-flux mechanism would allow warm anomalies in the deep ocean, and the associated high (steric) DSL anomalies, to be communicated onto the shelf via alongshore winds. Similarly for cool anomalies and low DSL anomalies. A qualitative upper bound on the role of this process in driving DSL on the NWES can be obtained by decomposing DSL, η, into a (dynamic) manometric component, η_m (Piecuch et al., 2022), and a steric component, η_s, such that

$$\eta = \eta_m + \eta_s, \tag{2}$$

with

$$\eta_m = \frac{1}{g\rho_s}p_b, \tag{3}$$

$$\eta_s = -\frac{1}{\rho_s}\int_{-H}^{0}\rho\,dz. \tag{4}$$

Here p_b is bottom pressure, g is the gravitational constant, ρ is density, ρ_s is density at the surface, and H is the depth of the bathymetry, with z the vertical coordinate. From the equation for the conservation of mass and the Boussinesq approximation we also have
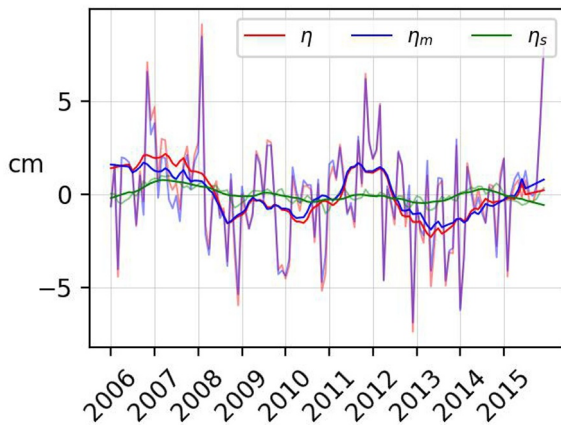
Figure 5. Shelf-mean dynamic sea level (red), shelf-mean dynamic manometric sea level (blue), and shelf-mean steric sea level (green), all from the reference experiment. Thick lines have had a 12-month rolling mean applied.

$$\eta_s = \int_{t_0}^{t} \int_{-H}^{0} \boldsymbol{u_3} \cdot (\nabla_3 \rho) \, dz \, dt', \quad (5)$$

where u_3 is the three-dimensional velocity and ∇_3 is the three-dimensional spatial derivative operator. Equation 5 says that the steric sea level anomaly is given by the cumulative depth-integrated advection of density. For a linear equation of state this can be decomposed into the advection of temperature and salinity. The steric component of DSL accounts for much more than just the wind-driven component of heat advection (it accounts for all horizontal density advection and surface fluxes), nevertheless, it is useful to see the proportion of DSL variance explained by this term.

Using the reference model output, Figure 5 shows that shelf-mean DSL variability on monthly to-interannual timescales is primarily associated with changes in η_m, that is, changes in the volume of water on the shelf are due to changes in the mass of water on the shelf rather than changes in the shelf-mean vertical integral of subsurface density. This suggests that cross-slope heat fluxes due to wind-driven Ekman transports are likely to be a smaller component of variability relative to wind-driven redistribution of mass on monthly to-interannual timescales. The manometric component has also been shown to be the dominant term in on-shelf DSL variability over interannual-to-decadal timescales (Bingham & Hughes, 2008; Dangendorf et al., 2021; Tinker et al., 2020; Vinogradova et al., 2007) and under climate forcing scenarios (Couldrey et al., 2021; Landerer et al., 2007).

This does not imply that wind-driven heat fluxes are unimportant at all spatial-temporal scales. For example, steric variability on the shelf region to the south of Ireland is more significant (see Figure S1 in Supporting Information S1) and the steric component is proportionally larger at the longer time scale in Figure 5 (and Figure S2 in Supporting Information S1), though still a small fraction of the total. Nevertheless, in the remainder of this paper we focus on the manometric component on monthly to-interannual timescales.

3.2.2. Remote Forcing

In the *bdy* experiment the model is forced with the variability in the lateral boundaries only. DSL variability in this case is defined here as being remotely forced. Tinker et al. (2020) and Hermans et al. (2020) found that on interannual-to-decadal timescales the lateral boundaries forced a spatially uniform mode of DSL variability on the shelf. We find the same is true for monthly variability. For example, Figure 4c shows that the leading EOF (85% of the variance) of DSL for the *bdy* experiment is mostly uniform across the shelf. Figure 4a compares the PCs for both the *nowind* and *bdy* experiments and shows that the leading modes have a consistent phase with a correlation of $r = 0.87$. Comparing Figures 4b and 4c shows that the leading mode EOFs for the two experiments both show uniform amplitudes across the shelf with similar magnitudes. This consistency suggests that the monthly variability in the *nowind* experiment, that is, which includes variability in local surface forcing (excluding wind), river, evaporation and precipitation and lateral boundary forcing, is dominated by the lateral boundary forcing contribution. In contrast, Hermans et al. (2020) showed that for interannual variability, the buoyancy flux contribution was at least as large as the lateral boundary contribution. This may be explained by the fact that the steric component of DSL variability increases at lower frequencies.

The relative importance of local and remote forcing on monthly to-interannual DSL variability can be estimated by seeing how much variance in the reference experiment DSL, η, can be explained by the locally generated DSL variance. For this we use the DSL from the experiment that used constant values at the lateral boundaries (*nobdy* experiment), η^{nobdy}. Figure 6a shows the variance explained in η by η^{nobdy}, and Figure 6b shows the same with 12-month rolling means applied to the time-series. The majority (80%–90%) of DSL variance in the North Sea is explained by local forcing, where winds are the dominant factor. Along the western portion of the shelf, however, the variance explained by local forcing is approximately 20% less. On the narrow shelves around Portugal and Spain and the edge of the shelf south or Ireland and west of France this drops below 50%. For the lower frequency variability represented by the 12-month rolling mean plots, the importance of remote forcing increases on the
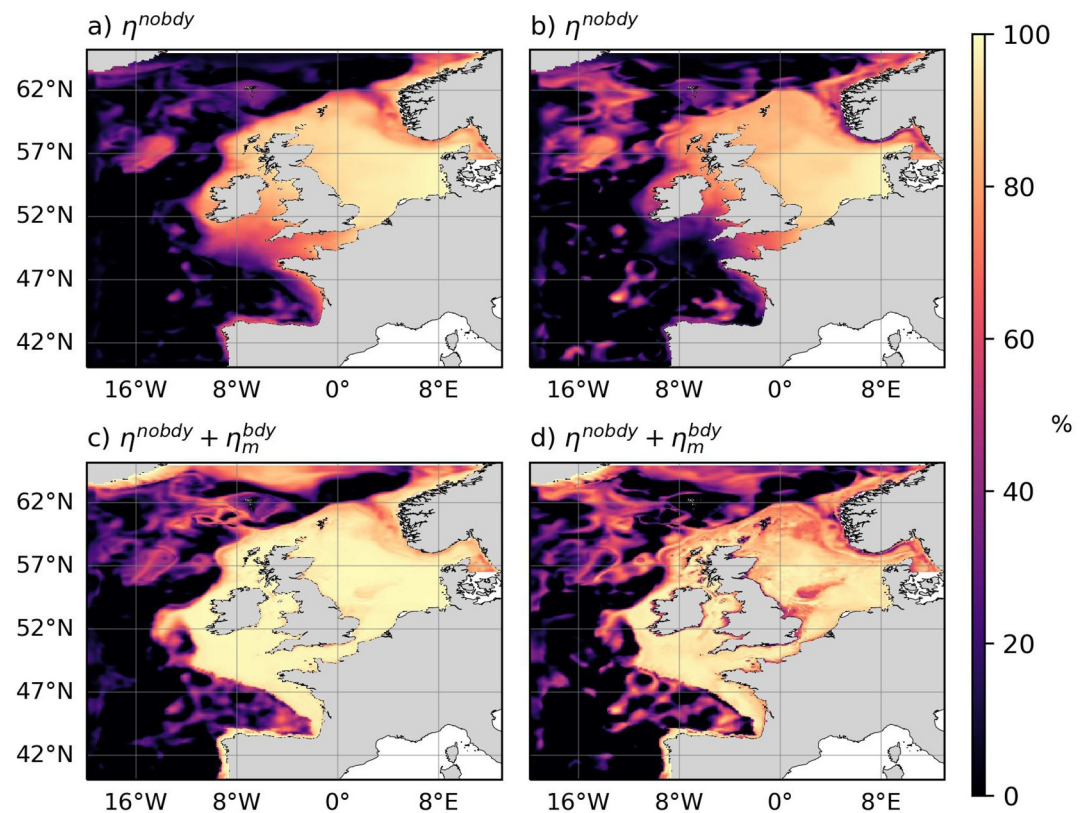
Figure 6. Percentage of variance explained in reference model dynamic sea level (DSL) by: (a) the DSL from the *nobdy* experiment, η^{nobdy}, and (c) the sum of the DSL from the *nobdy* experiment, η^{nobdy}, and the manometric sea level from the *bdy* experiment, η_m^{bdy}, that is, $\eta^{nobdy} + \eta_m^{bdy}$. Panels (b) and (d) show the same as (a) and (c), respectively, but with 12-month rolling means applied.

western and northern portions of the shelf. In most cases less than 30% of the variance is explained by the local forcing around Portugal, Spain and the shelf region south of Ireland.

Figure 6c shows the variance in η explained by $\eta^{nobdy} + \eta_m^{bdy}$, where η_m^{bdy} is the remotely forced manometric component of DSL. Figure 6d shows the same with 12-month rolling means applied first. Figures 6c and 6d shows that there is a remotely forced mass-flux onto the shelf that is important for explaining variance on the shelf on monthly to-interannual timescales - particularly along the narrow shelves around Portugal and Spain, as well as the shelves around France, Ireland, and southwest England. Note that this suggests that any remotely forced buoyancy fluxes across the shelfbreak are relatively unimportant to DSL on the NWES, that is, remotely forced steric variability is not required to explain DSL variance, the remote forcing is instead driving a convergence of water onto the shelf that increases the volume of the water-column. The importance of this mass-loading effect increases at the longer timescale. The effect also appears to be coherent along the southwestern and outer portion of the NWES.

3.2.3. Coherent Mode Along the North Atlantic Eastern Boundary

In the introduction we discussed the literature showing that DSL variability on the NWES can be coherent with larger-scale variability along the NAEB (e.g., Calafat et al., 2012; Chafik et al., 2017; Hogarth et al., 2020). We find that both the locally forced variability via the local winds, and the remotely forced variability, project onto larger-scale structures that cover the NAEB. Figure 7a shows the correlation between the PC of the second mode from the reference experiment (Figure 2b) and the SLA from altimetry. It shows that the anomaly extends from the western portion of the NWES along the Norwegian coast and into the Nordic Seas and Arctic Ocean. This is consistent with the near-uniform bottom pressure and sea level fluctuation investigated by Fukumori et al. (2015), which they attributed to wind-driven barotropic coastal trapped waves carrying NWES anomalies poleward.
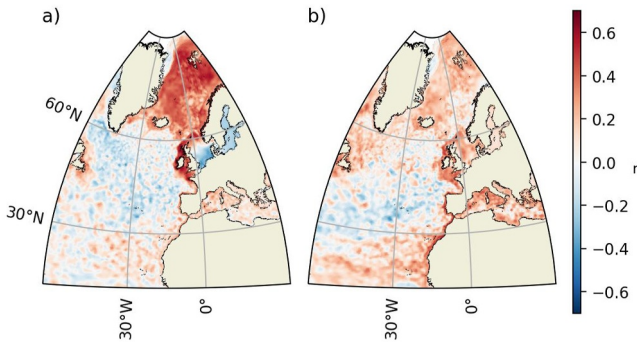
Figure 7. The North Atlantic eastern boundary (NAEB) mode. Panel (a) shows the correlation between altimetry derived sea level anomaly (SLA) and the Principle Component (PC) of mode 2 (NAEB) from the model reference run (Figure 2b). Panel (b) shows the correlation between the altimetry derived SLA, where an approximation of the signal associated with North West European Shelf local forcing has been removed, and the PC of the leading mode of manometric sea level variability from the *bdy* experiment, η_m^{bdy}.

To investigate this further we follow Calafat et al. (2012) by using an idealized representation of a wind-generated coastal trapped wave mode,

$$\xi(y,t) = \int_{y_0}^{y} B\tau_s\left(y', t - \frac{y-y'}{c}\right)dy', \qquad (6)$$

where y is the along isobath coordinate, y_0 is the latitude from which the integration begins, c is the wave speed, τ_s is the wind stress along the isobath and B is a coefficient controlling how much the mode is stimulated. Determining B is in general non-trivial, however, assuming a value of $B = 1$ means that the wave phase can be used for a nominal amplitude. Hughes et al. (2018) found a mode 1 (Kelvin) wave speed of 2.5 m/s at the equator, with faster speeds at higher latitudes. For an assumed wave speed of 3 m/s the wave will cross the 3,500 km distance between 40°N and 57°N along the shelf-edge in 13.5 days. For monthly mean sea level output, the wave adjustment is rapid and hence a comparison between Equation 6 and DSL from the model will be relatively insensitive to the value of c. For illustrative purposes, however, we note that using Equation 6 with the above values, we compute the wave by integrating the along-200-m-isobath wind stress from the bottom of our domain at $y_0 = 40°N$ to $y = 57°N$. The resulting correlation between ξ, and the mode 2 (NAEB) PC from the reference experiment is $r = 0.74$.

By performing the integration from 40°N we represent the cumulative wind-effect from within the domain, however, waves that originated at much lower latitudes can also propagate along the NWES. Figure 7b shows the correlation between the PC of the leading mode from the *bdy* experiment (remotely forced) and the SLA from altimetry, where we have first removed the projection of the locally forced signal from the SLA. This local signal is removed in three steps: (a) we perform an EOF decomposition on the DSL generated by the nobdy experiment (i.e., experiment with time-mean fields for lateral boundaries), (b) we use the six leading PCs (explaining >95% of the variance) as independent variables to create a multiple linear regression representation of the SLA (dependent variable) at every point on the altimetry grid and (c) remove this representation of the SLA from the actual SLA to give a modified SLA. The resulting correlation between the modified SLA and the remote mode of manometric sea level, η_m^{bdy}, shows coherence along the NAEB from the west coast of North Africa to much of the NWES. This represents remotely forced DSL variability due to changes in mass. This was shown to be important in Figures 6c and 6d. Combining the larger-scale projection of the remotely forced variability (Figure 7b) with the larger-scale projection from the local wind forced variability (Figure 7a) gives a mode covering the entire NAEB.

To understand the mechanism by which shelf-mean DSL is remotely forced and part of a larger NAEB mode, we require a physical description of how ocean dynamics at the shelf edge connects with the DSL.

3.3. Theoretical Framework

Starting from the equation describing the DSL tendency under the Boussinesq approximation,

$$\frac{\partial \eta}{\partial t} = F - \nabla \cdot \mathbf{U}, \qquad (7)$$

where F represents precipitation, evaporation and river run-off, and U = (U, V) is the horizontal depth integrated velocity $\mathbf{U} = \int_{-H}^{\eta}(u,v)dz$, with ∇ the horizontal derivative operator. We have seen from the similarity in DSL variability in the *nowind* and *bdy* experiments that removing precipitation, evaporation and river run-off has a small effect on shelf-mean DSL variability and we therefore simplify the following by neglecting the F term.

Horizontally integrating (Equation 7) across the surface area of the NWES, A, we can write the second term on the right of Equation 7 as $-\iint_A \nabla \cdot \mathbf{U}dA$. This region of shelf in our example is bounded by a curve C that consists of the 200 m isobath (C_{200}), two transects that connect the 200 m isobath with the coast (C_{Port} off-shore of Portugal, C_{Norw} connecting with the Norwegian Trench), and the coastline connecting the two transects (C_0). By applying the Divergence Theorem we then have
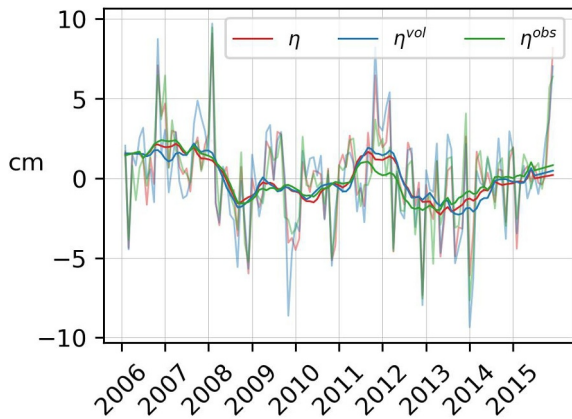
Figure 8. Shelf-mean dynamic sea level (red), cumulative volumetric flow onto the North West European Shelf (blue) (this is calculated using the cumulative divergence of the depth-integrated horizontal flow, integrated over the shelf, which is mathematically equivalent). These are the left (red) and right hand sides (blue) of Equation 10. Also shown is the shelf-mean absolute dynamic topography derived from altimetry (green). Thick lines have had a 12-month rolling mean applied.

$$-\iint_A \nabla \cdot \mathbf{U}\, dA = \oint_C \mathbf{U} \cdot \hat{\mathbf{n}}\, dc, \tag{8}$$

where $\hat{\mathbf{n}}$ is the unit vector into the shelf region A, and the term on the right is a closed integral along the curve C, which can be broken down into distinct sections. The equation for the change in the volume of water on the NWES is therefore

$$\iint_A \frac{\partial \eta}{\partial t} dA = \oint_C \mathbf{U} \cdot \hat{\mathbf{n}}\, dc, \tag{9}$$

which says that the tendency of shelf mean sea level is driven by the volumetric flow across the shelfbreak and the two cross-shelf transects, noting that the volumetric flow across the coastline connecting the two transects is zero. To obtain the DSL explicitly, we now integrate (Equation 9) over time to get

$$\iint_A \eta\, dA = \iint_A \eta_0\, dA + \int_0^t \oint_C \mathbf{U} \cdot \hat{\mathbf{n}}\, dc\, dt, \tag{10}$$

where η_0 is the initial DSL at the start of the integration. Using the reference model output, Figure 8 shows the left and right hand sides of Equation 10 for the NWES, both for the monthly mean and with a 12-month rolling mean applied. Figure 8 also shows the shelf-mean ADT derived from altimetry observations. We can see that the volumetric flow into the NWES does indeed closely reflect the variability in monthly to-interannual shelf-mean DSL variability in the model and observations.

To investigate the dynamic processes determining the volumetric flow across the shelfbreak, and thus shelf-mean DSL, we use three-dimensional momentum budgets from the model. The momentum budgets decompose the ocean current tendencies, that is, $\partial u / \partial t$, into the contributions from different ocean dynamic processes, where the momentum equation solved by the model is

$$\frac{\partial \mathbf{u}}{\partial t} = -f\mathbf{k} \times \mathbf{u} - \zeta \mathbf{k} \times \mathbf{u} - \frac{1}{2}\nabla(\mathbf{u}^2) - w\frac{\partial \mathbf{u}}{\partial z} - \frac{1}{\rho_0}\nabla p + D_h + D_v, \tag{11}$$

and on the right hand side, from left to right, the terms are: the Coriolis term, the relative vorticity contribution term, the kinetic energy gradient term, the vertical advection, the pressure gradient, the lateral diffusion, and the vertical diffusion, where w is the vertical velocity and ζ is the relative vorticity.

Each term is output from the model as a monthly mean. Over these time scales the tendency term is smoothed such that a first order balance can arise between the terms on the right of Equaion 11. The Coriolis term in Equaion 11 is then moved to the left hand side and by dividing through by f we have an equation giving the monthly mean contributions to $k \times u$. We then depth integrate, and rotate each term to a locally 200 m-isobath-following co-ordinate system to obtain a decomposition of the volume transport across the 200 m isobath at every grid point on the 200 m isobath (the heavy black line in Figure 1 excluding the short transects) as

$$\underbrace{\mathbf{U} \cdot \hat{\mathbf{n}}}_{U} = \underbrace{\overline{\zeta \mathbf{k} \times \mathbf{u}}}_{U_\zeta} + \underbrace{\overline{\frac{1}{2}\nabla(\mathbf{u}^2)}}_{U_{ke}} + \underbrace{\overline{w\frac{\partial \mathbf{u}}{\partial z}}}_{U_{ad}} + \underbrace{\overline{\frac{1}{\rho_0}\nabla(p)}}_{U_p} + \underbrace{\overline{D_h}}_{U_d} + \underbrace{\frac{1}{\rho_0 f}\hat{c} \cdot \boldsymbol{\tau}^s}_{U_s} + \underbrace{\frac{1}{\rho_0 f}\hat{c} \cdot \boldsymbol{\tau}^b}_{U_b}, \tag{12}$$

where the overline denotes the operation of depth integration divided by f, that is, $\overline{(-)} = \hat{c} \cdot \frac{1}{f}\int_{-H}^{\eta}(-)\, dz$. Here $\hat{n}$ is the cross-200 m-isobath unit vector and $\hat{c}$ is the along-200 m-isobath unit vector. The vertical integration of D_v has been expanded to give the individual contributions from along-isobath wind stress, $\hat{c} \cdot \boldsymbol{\tau}^s$, and along-isobath bottom stress, $\hat{c} \cdot \boldsymbol{\tau}^b$. We now integrate (Equation 12) along the 200 m isobath, $\int_{C_{200}} dc$, to give the individual
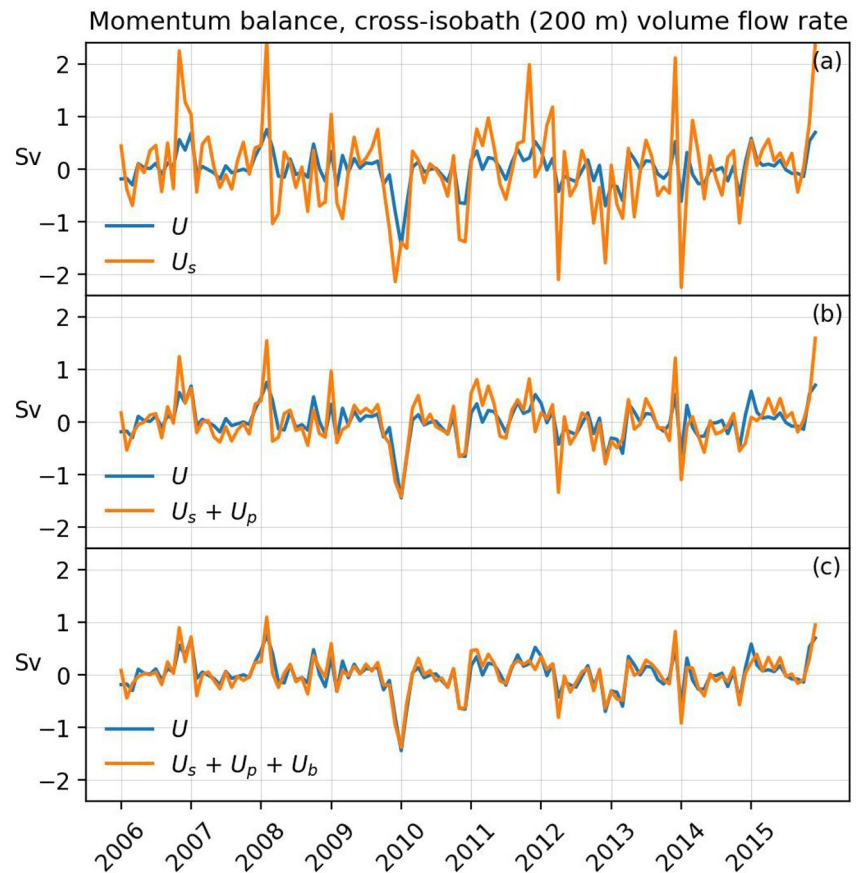
Figure 9. Reconstructions of the volumetric flow across the 200 m isobath of the North West European Shelf, U. Reconstruction in panel (a) uses only the surface Ekman transport U_s, panel (b) uses the surface Ekman transport plus the along-isobath pressure gradient component, U_p, panel (c) uses the surface Ekman transport plus the along-isobath pressure gradient component plus the bottom Ekman transport, U_b.

contributions to the total volume transport across the shelfbreak, and it should be assumed from this point onwards that we are always referring to along-isobath integrated quantities.

Note that unless explicitly stated otherwise, momentum budget analysis and transports refer to the reference experiment. Where we refer to transports from another experiment, we will provide the experiment name as a superscript, for example, U^{bdy} is the total volume transport across the 200 m isobath in the *bdy* experiment.

While we focus on the total transport across the shelfbreak (200 m isobath), the flow across the two transects, C_{Port} and C_{Norw}, also play a role. In both cases, the flow is geostrophic. For the reference run, the volume transport across C_{Port} has variability (as measured by the standard deviation) that is an order of magnitude smaller than the volume transport across the shelfbreak. This is partially due to the narrowness of the shelf in this region. The volume transport across the transect that connects with the Norwegian Trench, however, has a standard deviation (0.23 Sv) of the same order of magnitude as the standard deviation of transport across the shelfbreak (0.28 Sv), and is therefore important. We find the transport across C_{Norw} is anti-correlated with the transport across the shelfbreak ($r = -0.9$). The transport across C_{Norw} therefore tends to attenuate DSL variability driven by the addition of mass via the flow across the shelfbreak.

Figure 9 shows the total volume transport across the 200 m isobath, U, compared against three reconstructions (panels a–c) which each use different combinations of the terms on the right of Equation 12 for the reference experiment. Figure 9a compares U with the volume transport across the shelfbreak due to wind stress, U_s. The wind driven Ekman component is correlated with the total volume transport ($r = 0.74$), but the variance is an order of magnitude too large so that the percentage of variance explained by wind-driven Ekman transport using Equation 1
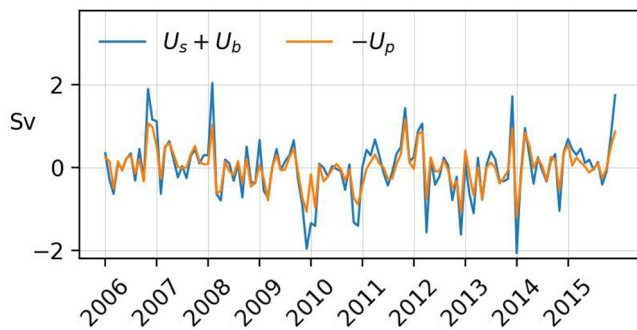
Figure 10. Comparison between the volumetric flow across the 200 m isobath due to surface plus bottom Ekman transport, $U_s + U_b$, and the volumetric flow off of the shelf due to the along-isobath pressure gradient component, $-U_p$.

is negative (this implies that the variance of $U - U_s$ is greater than the variance of U). Figure 9b compares U with the sum of the wind driven Ekman component and the along-isobath pressure gradient (geostrophic) term, U_p. This linear sum visually produces an improved reconstruction with an increased correlation ($r = 0.79$), however the percentage of variance explained using Equation 1 remains negative because the variance is still too large. Figure 9c shows the reconstruction when the bottom Ekman transport term, U_b, is linearly added. It now shows a very skilful reconstruction with correlation $r = 0.89$ and with 73% of the variance explained. Note that this is not to suggest that bottom stress is more important than the wind and pressure gradient contributions—all three contributions are required together. The important point of this result is that, while surface Ekman transport is correlated with DSL on the NWES, it is not sufficient to explain the variability in DSL on the NWES.

Geostrophic transport, U_p, is an important component of the flow across the shelf edge. The variability in this component accounts for the effects of local and remote dynamics on the pressure field. We find that the domain-local winds are a major driver of this pressure gradient. Figure 10 shows that the integrated pressure gradient along the 200 m isobath is in anti-phase with the combined integrated surface and bottom Ekman transports (correlation coefficient is $r = -0.93$). The mechanism depends on the generation of wind driven coastal trapped waves (e.g. Allen, 1980; Brink, 1991; Middleton & Leth, 2004). Specifically, wind generated coastal trapped waves are a consequence of the Ekman transport across isobaths, which produces a compensating flow to conserve mass and this results in vortex stretching and local changes in relative vorticity. The vorticity dynamics are expressed via the along-shore velocity and where there is along-isobath variability, waves propagate the anomalies along the continental slope and shelf. The propagation and decay of coastal trapped waves (an Arrested Topographic Wave (Csanady, 1978) when the time scale of adjustment is rapid relative to the time scale of forcing variability) establishes a new equilibrium with an along-shore pressure gradient balanced by a cross-shore flow that offsets the surface Ekman transport. This process is analogous to the set up of Sverdrup balance by Rossby waves in response to Ekman pumping. Whereas Rossby waves propagate east to west, the coastal trapped waves at the continental slopes are constrained by the topography (topographic Rossby waves), which would set up a topographic Sverdrup balance. An additional factor here, however, is that bottom friction is playing a role, which can affect the topographic Rossby wave propagation (Wise, Hughes, et al., 2020) and the flow and pressure gradient that is set up (Wise et al., 2018).

As demonstrated in the previous section, the amplitude of the wave can be represented by an along-shore integral of the along-shore wind stress. The correlation between the along-200 m-isobath wind stress integrated from 40° to 57°N, as discussed in the previous section, and the along-200 m-isobath pressure gradient at 57°N is $r = -0.69$.

It is typical that investigations into shelfedge transports, boundary waves and sea level occur separately. As we have shown here, however, the relationship between them is important to understanding the mechanisms driving DSL variability on the shelf. This is important for the NWES where cross-shelfedge volume transports are large (Huthnance et al., 2022), but it is also relevant for timescales and regions other than those considered here. Indeed, Thompson and Mitchum (2014) used a form of Equation 10 to investigate alongshore coherence in DSL along the US east coast on interannual-to-decadal timescales using model output. Their analysis of the driving mechanism was limited by not having access to the individual terms driving variability in the transport onto the shelf (and their 1° model output meant that transports could only be considered as cross-slope in a very rough sense). Separately from investigations of sea level, a number of studies have investigated momentum balances on other shelves in a range of contexts and demonstrated the importance of alongshore wind as a driver of the alongshore pressure gradient and cross-shelf geostrophic flow (e.g., Fewings & Lentz, 2010; Lentz et al., 1999; Tyler & Sanderson, 1996). However, as Xu and Oey (2011) demonstrated along the US east coast, non-local drivers, such as Labrador Sea inflows, can act to remotely set-up an alongshore pressure gradient. Similarly, remote forcing has been identified as an important driver of shelf circulation on the NWES on seasonal (Holt & Proctor, 2008) and future climate (Holt et al., 2018) timescales.

When the domain local winds are removed, a pressure gradient along the 200 m isobath remains. This reflects remote variability that is entering via the lateral boundaries either directly from the deep ocean, or along the continental boundary, from lower latitudes. Figure 11 shows the along-isobath (200 m) pressure gradient for the
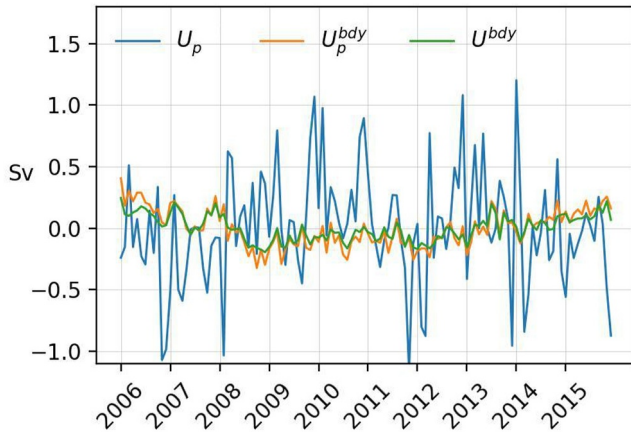
Figure 11. Volumetric flow across the 200 m isobath due to the along-isobath pressure gradient in the reference experiment, U_p, and *bdy* experiment, U_p^{bdy}. Also shown is the total volumetric flow across the 200 m isobath in the *bdy* experiment, U^{bdy}.

ref and *bdy* experiments, as well as the total cross-isobath volumetric flow for the *bdy* experiment. First, it shows that variability in the pressure gradient remains when local forcing is removed, but that it is reduced in magnitude, specifically the standard deviation is reduced from 0.45 to 0.15 Sv. Second, the Figure shows that in contrast to the reference case, the pressure gradient accounts for the majority of the cross-isobath volumetric flow variability when local winds are removed (percentage of variance explained is 62%). Note that while ageostrophic terms are relatively unimportant in the cross-isobath volumetric flow in this case, they are important in terms of the vorticity, which ultimately acts as a constraint on the pressure field. See for example, the effect of bottom friction on the coastal trapped waves and along-shore pressure gradient when solving the vorticity equation in Wise, Hughes, et al. (2020) and Wise et al. (2018).

We can now expand the right hand side of Equation 10 to obtain a leading order equation for the cross-isobath volume transport:

$$\mathbf{U} \cdot \hat{\mathbf{n}} = \hat{\mathbf{c}} \cdot \frac{1}{f\rho_0}\left[\int_{-H}^{\eta} \nabla\left(p^{loc} + p^{rem}\right) dz + \boldsymbol{\tau}_s - \boldsymbol{\tau}_b\right], \tag{13}$$

where $\hat{\mathbf{c}}$ is the unit vector along the 200 m isobath and $\hat{\mathbf{n}}$ is the unit vector across it, and where p^{loc} is the locally generated pressure and p^{rem} the remotely generated pressure.

As previously demonstrated in Figure 10, the variability in the local component of pressure is closely associated with the local wind stress. We find that a linear regression of the wind stress term onto the pressure gradient using the *nobdy* experiment output allows us to reconstruct the local pressure term from the (local) wind stress term explaining 88% of the variance. The regression coefficient is $\alpha_p = -0.5$. Using this regression coefficient in Equation 13 gives

$$\mathbf{U} \cdot \hat{\mathbf{n}} = \hat{\mathbf{c}} \cdot \frac{1}{f\rho_0}\left[\int_{-H}^{\eta} \nabla p^{rem} dz + 0.5\boldsymbol{\tau}_s - \boldsymbol{\tau}_b\right], \tag{14}$$

where the constant $0.5 = (1 + \alpha_p)$. Note that we also find that using the same regression approach the local wind stress can explain a large fraction of the variance due to bottom friction (62 %, regression coefficient $\alpha_b = -0.15$). Hence bottom friction can also be separated into remote and local contributions, although in this case a larger proportion of the local variability is unexplained.

From the remotely forced *bdy* experiment we know that the remote geostrophic component–the first term on the right hand side of Equation 14 is related to a relatively spatially uniform mode of variability on the shelf. The remote geostrophic component (across the shelfbreak and transect between Denmark and Norwegian Trench) is approximately equivalent to a shelf-mean DSL standard deviation of 2 cm (using the *bdy* experiment DSL). This compares to the reference run where the equivalent standard deviation is 3 cm (see Figure S2 in Supporting Information S1).

3.4. Mass Loading Via East Atlantic Boundary Propagation

Frederikse et al. (2016) hypothesized that the correlation between on-shelf manometric sea level and off-shelf steric variability in the Bay of Biscay may result from both being forced by wind stress generated coastal trapped waves that propagate poleward along the boundary and also westward as Rossby waves. Within our framework, this implies that the source of remote pressure variability is from lower latitudes rather than directly from the adjacent ocean.

To test whether variability is entering the domain from the south along the continental boundary we use the *bdy_block_ctw* experiment. The *bdy_block_ctw* experiment applies 10-year mean fields at the lateral boundary between the deep ocean and the coast of Portugal (12°–8°W at 40°N). This blocks remotely generated variability that is propagating northward along the continental boundary toward the NWES. The variance in η_m^{bdy} explained
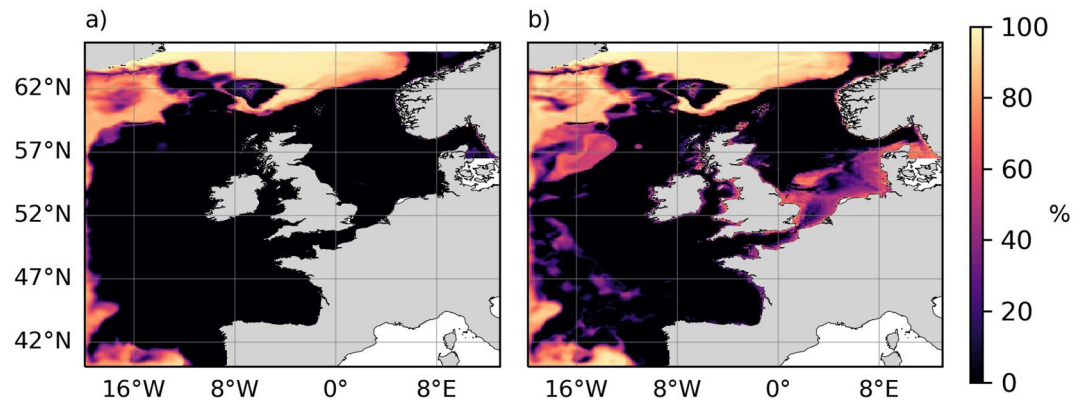
Figure 12. Panel (a) shows the percentage of variance explained in the manometric sea level from the *bdy* experiment, η_m^{bdy}, by the manometric sea level from the *bdy_block_ctw* experiment, $\eta_m^{bdy\_block\_ctw}$. In the *bdy_block_ctw* experiment the southern lateral boundary is held constant close to the coast of Portugal (see red line in Figure 1). Panel (b) shows the same as (a) but with a 12-month rolling mean applied.

by $\eta_m^{bdy\_block\_ctw}$ (the manometric sea level from the *bdy_block_ctw* experiment) gives a measure of the sensitivity of remote forcing to variability entering along the continental boundary.

Figure 12a shows the percentage of variance in η_m^{bdy} explained by $\eta_m^{bdy\_block\_ctw}$, and Figure 12b shows the same with 12-month rolling means applied. Close to zero percent of the remotely generated variability on the shelf can be explained when the small section of lateral boundary is held constant. The majority of the variability in manometric sea level in the deep ocean to the west of the shelf is also unexplained. Although note that Figure 12b also shows that at least 50% of the variance in the Southern North Sea remains explained. This suggests that an important source of variability enters from the lateral boundary to the east of Denmark (Kattegat Sea), which links the NWES with the Baltic Sea. Nevertheless, Figure 12 implies that an important source of variability enters from the south, along the continental boundary, and propagates around the shelf, influencing sea level on the NWES. There is also evidence of a separation of the propagating signal (inferred from the region of 0% explained variance) into two branches at the Wyville Thomson Ridge (north west of Scotland), which is where the bathymetry forks. This is reminiscent of the mechanism described in Fukumori et al. (2015) for propagating waves exciting the Arctic mode of bottom pressure variability (their Figure 11).

Note that while Figure 12 implies boundary trapped sources of variability are important, it does not imply that forcing from other sections of the lateral boundary are strictly unimportant. In particular, Hermans et al. (2020) found that on interannual timescales, both the southern and western lateral boundaries of their NWES regional model forced DSL variability on the shelf with similar magnitude standard deviations. It is likely therefore that they modulate one another. A larger domain model could be used to investigate this further.

To investigate whether the remote forcing from the south is potentially due to remote winds, we look at the relationship between η_m^{bdy} and a subsection of remote alongshore winds (recall that η_m^{bdy} is generated by an experiment without any local forcing). Figure 13 shows the correlation between η_m^{bdy} and the average meridional wind stress between 38 and 40 N and 12-8 W from the ERA5 data set. Although, this is a very small fraction of the region where along-shore wind stress might generate coastal trapped waves, Figure 13 shows a clear positive correlation on the shelf that is in-phase. This suggests that remote along-shore wind stress could be a driver of the remote mode of variability on the NWES, however since we cannot control for other drivers of the lateral boundary that may also be correlated with the along-shore wind, this does not prove causation.

The final component of the Frederikse et al. (2016) hypothesis is that the remotely generated on-shelf variability is associated with steric variability in the Bay of Biscay due to the radiation of Rossby waves. Figures 14a and 14b show the correlation between Bay of Biscay-mean η_s and η_m at every grid point for the *bdy* and *bdy_block_ctw* experiments, respectively. Contrasting Figures 14a and 14b shows that the correlation on the shelf reduces dramatically when we block the remote variability from the south near the coast of Portugal. The shelf-average reduction in r^2 is 61%. This result is consistent with both η_s in the Bay of Biscay and η_m on the shelf resulting from the same remote cause, rather than η_s in the Bay of Biscay driving η_m on the shelf.
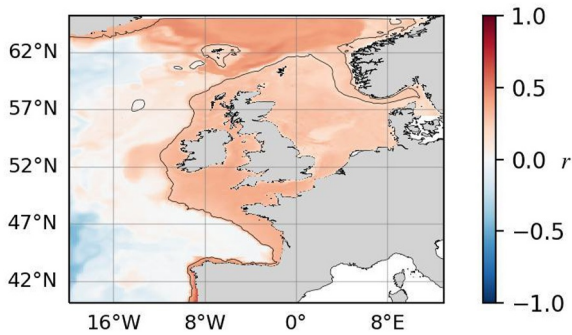
Figure 13. Correlation between manometric sea level from the *bdy* experiment, η_m^{bdy}, with remote meridional wind stress averaged over 38–40 N and 12-8 W from the ERA5 data set.

In summary, there is evidence for the hypothesis that remote wind generated waves entering the domain from the south are important in establishing the new equilibrium and pressure anomalies that produce along-isobath pressure gradients, $\hat{\mathbf{c}} \cdot \nabla p^{rem}$. This pressure gradient is balanced by a geostrophic flow onto the shelf. The integral of this flow around the NWES is the net volumetric flow onto the shelf on monthly timescales, which produces the shelf-mean manometric and dynamic sea levels. Over a 10-year period the resulting monthly mean detrended and deseasonalized standard deviation in DSL is 2 cm. In addition to remote winds, other processes are potentially driving the pressure gradient. For example, gyre related variability due to wind stress curl in the interior ocean could result in a pressure signal that propagates equatorward along the western boundary of the North Atlantic and eastward along the equatorial wave guide and then poleward along the eastern boundary. This mechanism has been described for a 1.5 layer model by Johnson and Marshall (2002) in relation to the AMOC. On longer timescales interior ocean dynamics could also be important for the along-isobath pressure gradient via density anomalies transported toward the continental slope. These factors require further investigation using a model covering the North Atlantic.

4. Conclusion

In this study we have used sensitivity experiments and monthly mean momentum budget diagnostics from an ocean circulation model simulating 2006–2015 to investigate mechanisms of DSL variability on the NWES over monthly to-interannual timescales.

The model captures the modes of shelf sea variability seen in observations, both offshore and coastal. DSL variability on the shelf is dominated by mass variations, with steric signals relatively small (although there are regional exceptions away from the coast). Regional variations in shelf DSL are predominately caused by local winds.

Our key findings for monthly to-interannual variability are that:

- For local forcing (not from lateral boundaries), the net mass flux onto the shelf, which produces a shelf-mean change in DSL, results from a combination of surface Ekman, bottom Ekman, and geostrophic flows responding to the winds, which are closely related to each other, with the geostrophic flow opposing the surface Ekman flux with approximately half the transport.
- Remote forcing (from the lateral boundaries) produces a DSL mode which is almost uniform over the shelf and results mostly from mass-fluxes onto the shelf, rather than buoyancy fluxes.
- This net mass flux onto the shelf is dominated by the geostrophic component, with bottom friction playing an important indirect role.
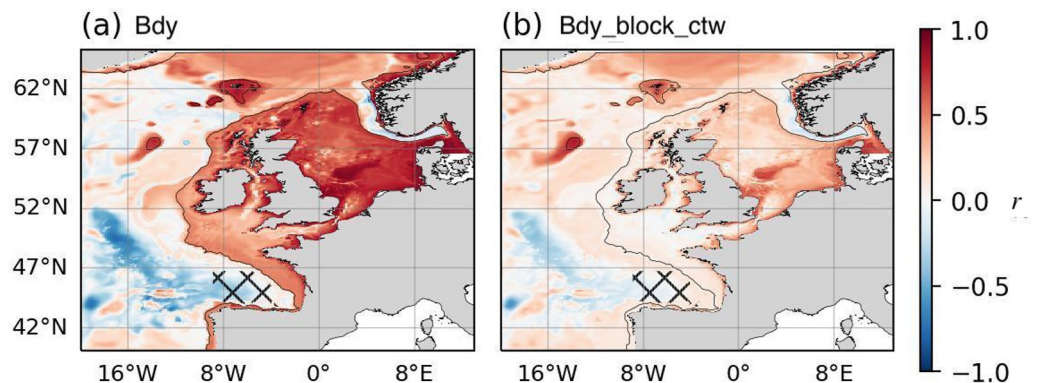

Figure 14. Correlation between steric sea level, η_s, meaned over the Bay of Biscay (region denoted with hatches) and manometric sea level, η_m, at every grid point, both for (a) the *bdy* experiment and (b) the *bdy_block_ctw* experiment.

- The remote forcing responsible for this mode is highly sensitive to signals propagating into the domain from the southern boundary, near to the Portuguese coast, as expected of a coastal-trapped wave signal. This mode is particularly important for explaining DSL variance along the western portion of the NWES.
- The same remote forcing also appears to be the cause of the steric sea level signal in the Bay of Biscay which is related to shelf sea level.
- The local wind dominated mode and the remote mode, which is correlated with remote winds, form part of a larger NAEB mode extending from north Africa to the Arctic.

More specifically, excluding the effects of atmospheric pressure, which can be accounted for by an inverse barometer response, local winds drive the majority of monthly to-interannual DSL variability on the NWES. Removing the winds from a NWES regional model without the inverse barometer effect reduces the average variance by 82%. Local winds are responsible for driving a North Sea mode of variability that is characterized by intensified in-phase variability along the coasts of Germany, the Netherlands and Denmark, with an amplitude extreme of approximately 30 cm. The along-shore winds also drive a NAEB mode, which is characterized by in-phase variability along the western and northern extents of the shelf. In the model this mode extends along the shelf from Portugal to Norway with an amplitude extreme of approximately 15 cm and, using satellite altimetry, the mode is shown to extend from North Africa to the Arctic (with an implied phase lag). This is consistent with a number of studies identifying a mode along the eastern boundary (e.g., Calafat et al., 2012; Fukumori et al., 2015; Hogarth et al., 2020). These spatial patterns result from wind-forced volume redistribution on the shelf, and also from a loading of water from the deeper ocean onto the shelf. Because the variability in DSL on the shelf is explained by dynamic manometric sea level, that is, non-steric, we take this to imply a limited role for wind-driven heat fluxes as a driver of monthly DSL variability.

Shelf-mean DSL variability on the NWES is largely driven by changes in horizontal volume transport into the region. Using momentum budget diagnostics we find that the sum of surface, U_s, and bottom, U_b, Ekman transport, and geostrophic transport, U_p, explain 73% of the variance in total volume transport across the shelf-edge, U. Surface Ekman transport is insufficient as a mechanistic description of this DSL variability. The along-shore winds are reflected in the pressure field along the shelf-edge and hence the local geostrophic transport onto the shelf, U_p^{loc}, where the geostrophic component has been split into locally and remotely generated components, $U_p = U_p^{loc} + U_p^{rem}$. When integrated along the shelf-edge, the local geostrophic transport opposes the surface Ekman transport, and we find that 82% of the variance in the local geostrophic transport can be explained using the approximation $U_p^{loc} = -0.5U_s$. Covariance-based statistical approaches might result in the geostrophic transport component being interpreted as part of the surface Ekman transport. This highlights the advantage of physics based models in cases where the contributing processes are all correlated with one another.

Along-shore winds can result in vortex stretching and local changes in relative vorticity via flow crossing isobaths, this generates coastal trapped waves that propagate velocity and pressure anomalies along the boundary. Using an analytical coastal trapped wave model we find that integrating the along-isobath (200 m) winds along the western portion of the shelf, from 40°N to 57°N, produces a nominal wave mode amplitude with variability that is highly correlated with the NAEB mode ($r = 0.74$). The pressure gradient at 57°N is correlated with the wave mode with correlation coefficient $r = -0.69$. As the waves propagate along the boundary, thus establishing a new equilibrium, they produce pressure gradients and hence cross-isobath flow which is responsible for setting up the sea level signal and which is the result of the adjustment process.

When local forcing is removed from the model, that is, forcing the model using only the lateral boundary variations, a remote geostrophic transport across the shelf edge, U_p^{rem}, remains. It explains 62% of the variance in the remaining volume transport across the shelf-edge, and this drives a mode of DSL variability on the NWES with a 2 cm shelf-mean standard deviation. This remote mode is relatively spatially uniform, it is highly sensitive to variability propagating poleward along the eastern boundary, and it is correlated with remote (lower-latitude) along-shore winds. This remotely generated variability, which forks at the Wyville Thomson Ridge (north west of Scotland) with Icelandic and Norwegian branches, forms part of the NAEB mode. Its uniformity on the NWES makes it a strong candidate as an explanation of the common mode in UK tide gauges identified by Hogarth et al. (2020). This remote mode is also particularly important for explaining the variability in DSL along the western portion of the shelf, with the local forcing explaining typically less than 30% of the interannual variance in DSL along the shelves around Portugal, Spain, western France, southern/western

Ireland, and southwest England. Linearly adding the mass loading effect of the remote forcing brings this up to at least 90%.

In previous studies it has been found that steric height in the Bay of Biscay is correlated with manometric sea level on the NWES. The direction of causality has not been clear, however Frederikse et al. (2016) hypothesized that the correlation could result from wind generated coastal trapped waves. These waves propagate poleward along the boundary, modifying DSL on the NWES, while also radiating away from the boundary as Rossby waves and modifying off-shelf steric height. We found that blocking variability from propagating along the boundary at 40°N, off the coast of Portugal, reduced the average squared correlation between steric height in the Bay of Biscay and manometric sea level on the NWES by 61%. This is consistent with Bay of Biscay steric height and NWES sea level having a common cause, rather than Bay of Biscay steric height causing NWES sea level to change.

In this study we have focused on monthly to-interannual timescales and how local and remote winds drive DSL on the NWES over the period 2006–2015. The close association between winds and sea level has been discussed in the literature over longer time periods (see introduction), however a caveat to our own conclusions is that the relative importance of forcing terms can change over time. A longer set of experiments than conducted here would be required to determine the importance of any such change. This point notwithstanding, our conclusions and results have broader implications for DSL variability attribution on the NWES.

Firstly, the importance of remotely forced DSL on the southwestern portion of the NWES due to mass-loading, which depends on the pressure derived from the boundaries of the domain, suggests that studies focused on quantitative DSL sensitivity to lateral boundary data sets and conditions in isolation would be beneficial to regional modelers.

Secondly, causally quantifying the effect on coastal DSL of large-scale ocean variability, such as that associated with the AMOC, depends on filtering out the large effects of local and remote along-shore winds. For example, Brunnabend et al. (2014) used hosing experiments to isolate AMOC variability over a 50 year period and showed a link between a slowing AMOC and DSL increases on the NWES. As demonstrated here, the large effects of winds manifest partially in the along-shore pressure gradient and geostrophic flow across the shelf-edge. However, it is expected that the redistribution of water from the deep ocean to the shelf, due to large-scale ocean dynamics, should also affect the along-shore pressure gradient balanced flow as a result of boundary wave propagation (e.g., Hughes et al., 2019). For example, changes in interior Sverdrup balance propagate toward the western boundary, where they can be communicated to the NWES via coastal trapped waves and the equatorial wave guide. This pathway has previously been demonstrated for surface layer thickness in response to AMOC variability by Johnson and Marshall (2002) using a 1.5 layer model. Relative to the winds, such a remote oceanic signal (representing the signature of AMOC variability on coastal sea level) might be small, and thus difficult to detect without first removing the along-shore wind effects. The approach and theoretical framework developed in this study will be useful for extending our results beyond monthly to-interannual timescales to identify the mechanisms and quantify the effect of large-scale and lower frequency ocean variability on NWES sea level.

Data Availability Statement

Model data required to reproduce the research are available from (Wise, Calafat, et al., 2024). The AMM7 model configuration and source code is available from (Wise, Polton, & Harle, 2024). Tide gauge data is available from Permanent Service for Mean Sea Level (2022) (Holgate et al., 2013). Sea level anomaly and ADT data sets are available from (CMEMS, 2023a; CMEMS, 2023b), respectively. The ERA5 data set is available from (Hersbach et al., 2018).

References

Allen, J. (1980). Models of wind-driven currents on the continental shelf. *Annual Review of Fluid Mechanics*, *12*(1), 389–433. https://doi.org/10.1146/annurev.fl.12.010180.002133

Bingham, R. J., & Hughes, C. W. (2008). The relationship between sea-level and bottom pressure variability in an eddy permitting ocean model. *Geophysical Research Letters*, *35*(3), 1–5. https://doi.org/10.1029/2007GL032662

Brink, K. H. (1991). Coastal-trapped waves and wind-driven currents over the continental shelf. *Annual Review of Fluid Mechanics*, *23*(1), 389–412. https://doi.org/10.1146/annurev.fl.23.010191.002133

Bruciaferri, D., Shapiro, G. I., & Wobus, F. (2018). A multi-envelope vertical coordinate system for numerical ocean modelling. *Ocean Dynamics*, *68*(10), 1239–1258. https://doi.org/10.1007/s10236-018-1189-x

Brunnabend, S.-E., Dijkstra, H., Kliphuis, M., van Werkhoven, B., Bal, H., Seinstra, F., et al. (2014). Changes in extreme regional sea surface height due to an abrupt weakening of the Atlantic meridional overturning circulation. *Ocean Science*, *10*(6), 881–891. https://doi.org/10.5194/os-10-881-2014

Calafat, F. M., Chambers, D. P., & Tsimplis, M. N. (2012). Mechanisms of decadal sea level variability in the eastern North Atlantic and the Mediterranean Sea. *Journal of Geophysical Research*, *117*(9), 1–14. https://doi.org/10.1029/2012JC008285

Chafik, L., Nilsen, J. E. Ø., & Dangendorf, S. (2017). Impact of North Atlantic teleconnection patterns on Northern European sea level. *Journal of Marine Science and Engineering*, *5*(3), 43. https://doi.org/10.3390/jmse5030043

Chafik, L., Nilsen, J. E. Ø., Dangendorf, S., Reverdin, G., & Frederikse, T. (2019). North Atlantic Ocean circulation and decadal sea level change during the altimetry era. *Scientific Reports*, *9*(1), 1–9. https://doi.org/10.1038/s41598-018-37603-6

CMEMS. (2023a). SEALEVEL_EUR_PHY_L4_MY_008_068 [Dataset]. *E.U. Copernicus Marine Service Information (CMEMS). Marine Data Store (MDS)*. https://doi.org/10.48670/moi-00141

CMEMS. (2023). SEALEVEL_GLO_PHY_L4_MY_008_047 [Dataset]. *E.U. Copernicus Marine Service Information (CMEMS). Marine Data Store (MDS)*. https://doi.org/10.48670/moi-00148

Couldrey, M. P., Gregory, J. M., Boeira Dias, F., Dobrohotoff, P., Domingues, C. M., Garuba, O., et al. (2021). What causes the spread of model projections of ocean dynamic sea-level change in response to greenhouse gas forcing? *Springer Berlin Heidelberg*, *56*(1–2), 155–187. https://doi.org/10.1007/s00382-020-05471-4

Csanady, G. (1978). The arrested topographic wave. *Journal of Physical Oceanography*, *8*(1), 47–62. https://doi.org/10.1175/1520-0485(1978)008<0047:tatw>2.0.co;2

Dangendorf, S., Calafat, F. M., Arns, A., Wahl, T., Haigh, I. D., & Jensen, J. (2014). Mean sea level variability in the North Sea: Processes and implications. *Journal of Geophysical Research: Oceans*, *119*(10), 6820–6841. https://doi.org/10.1002/2014jc009901

Dangendorf, S., Frederikse, T., Chafik, L., Klinck, J. M., Ezer, T., & Hamlington, B. D. (2021). Data-driven reconstruction reveals large-scale ocean circulation control on coastal sea level. *Nature Climate Change*, *11*(6), 514–520. https://doi.org/10.1038/s41558-021-01046-1

Fewings, M. R., & Lentz, S. J. (2010). Momentum balances on the inner continental shelf at Martha's Vineyard Coastal Observatory. *Journal of Geophysical Research*, *115*(C12), C12023. https://doi.org/10.1029/2009jc005578

Flather, R. (1976). A tidal model of the northwest European continental shelf. *Mémoires de la Société Royale des Sciences de Liège*, *10*, 141–164.

Frederikse, T., Riva, R., Kleinherenbrink, M., Wada, Y., van den Broeke, M., & Marzeion, B. (2016). Closing the sea level budget on a regional scale: Trends and variability on the northwestern European continental shelf. *Geophysical Research Letters*, *43*(20), 10864–10872. https://doi.org/10.1002/2016gl070750

Fukumori, I., Wang, O., Llovel, W., Fenty, I., & Forget, G. (2015). A near-uniform fluctuation of ocean bottom pressure and sea level across the deep ocean basins of the Arctic Ocean and the Nordic Seas. *Progress in Oceanography*, *134*, 152–172. https://doi.org/10.1016/j.pocean.2015.01.013

Good, S. A., Martin, M. J., & Rayner, N. A. (2013). En4: Quality controlled ocean temperature and salinity profiles and monthly objective analyses with uncertainty estimates. *Journal of Geophysical Research: Oceans*, *118*(12), 6704–6716. https://doi.org/10.1002/2013jc009067

Hannachi, A., Jolliffe, I. T., & Stephenson, D. B. (2007). Empirical orthogonal functions and related techniques in atmospheric science: A review. *International Journal of Climatology: A Journal of the Royal Meteorological Society*, *27*(9), 1119–1152. https://doi.org/10.1002/joc.1499

Hermans, T. H., Katsman, C. A., Camargo, C. M., Garner, G. G., Kopp, R. E., & Slangen, A. B. (2022). The effect of wind stress on seasonal sea-level change on the northwestern European shelf. *Journal of Climate*, *35*(6), 1745–1759. https://doi.org/10.1175/jcli-d-21-0636.1

Hermans, T. H., Le Bars, D., Katsman, C. A., Camargo, C. M., Gerkema, T., Calafat, F. M., et al. (2020). Drivers of interannual sea level variability on the northwestern European shelf. *Journal of Geophysical Research: Oceans*, *125*(10), e2020JC016325. https://doi.org/10.1029/2020jc016325

Hersbach, H., Bell, B., Berrisford, P., Biavati, G., Horányi, A., Muñoz Sabater, J., et al. (2018). ERA5 hourly data on single levels from 1979 to present [Dataset]. *Copernicus Climate Change Service (C3S) Climate Data Store (CDS)*. https://doi.org/10.24381/cds.adbb2d47

Hogarth, P., Hughes, C., Williams, S., & Wilson, C. (2020). Improved and extended tide gauge records for the British Isles leading to more consistent estimates of sea level rise and acceleration since 1958. *Progress in Oceanography*, *184*, 102333. https://doi.org/10.1016/j.pocean.2020.102333

Holgate, S. J., Matthews, A., Woodworth, P. L., Rickards, L. J., Tamisiea, M. E., Bradshaw, E., et al. (2013). New data systems and products at the permanent service for mean sea level. *Journal of Coastal Research*, *29*(3), 493–504.

Holt, J., Polton, J., Huthnance, J., Wakelin, S., O'dea, E., Harle, J., et al. (2018). Climate-driven change in the north Atlantic and arctic oceans can greatly reduce the circulation of the North Sea. *Geophysical Research Letters*, *45*(21), 11–827. https://doi.org/10.1029/2018gl078878

Holt, J., & Proctor, R. (2008). The seasonal circulation and volume transport on the Northwest European continental shelf: A fine-resolution model study. *Journal of Geophysical Research*, *113*(C6), C06021. https://doi.org/10.1029/2006jc004034

Hong, B., Sturges, W., & Clarke, A. J. (2000). Sea level on the US East Coast: Decadal variability caused by open ocean wind-curl forcing. *Journal of Physical Oceanography*, *30*(8), 2088–2098. https://doi.org/10.1175/1520-0485(2000)030<2088:slotus>2.0.co;2

Hughes, C. W., Fukumori, I., Griffies, S. M., Huthnance, J. M., Minobe, S., Spence, P., et al. (2019). Sea level and the role of coastal trapped waves in mediating the influence of the open ocean on the coast. *Surveys in Geophysics*, *40*(6), 1467–1492. https://doi.org/10.1007/s10712-019-09535-x

Hughes, C. W., Tamisiea, M. E., Bingham, R. J., & Williams, J. (2012). Weighing the ocean: Using a single mooring to measure changes in the mass of the ocean. *Geophysical Research Letters*, *39*(17), L17602. https://doi.org/10.1029/2012gl052935

Hughes, C. W., Williams, J., Blaker, A., Coward, A., & Stepanov, V. (2018). A window on the deep ocean: The special value of ocean bottom pressure for monitoring the large-scale, deep-ocean circulation. *Progress in Oceanography*, *161*, 19–46. https://doi.org/10.1016/j.pocean.2018.01.011

Huthnance, J., Hopkins, J., Berx, B., Dale, A., Holt, J., Hosegood, P., et al. (2022). Ocean shelf exchange, NW European shelf seas: Measurements, estimates and comparisons. *Progress in Oceanography*, *202*, 102760. https://doi.org/10.1016/j.pocean.2022.102760

Johnson, H. L., & Marshall, D. P. (2002). A theory for the surface Atlantic response to thermohaline variability. *Journal of Physical Oceanography*, *32*(4), 1121–1132. https://doi.org/10.1175/1520-0485(2002)032<1121:atftsa>2.0.co;2

Landerer, F. W., Jungclaus, J. H., & Marotzke, J. (2007). Ocean bottom pressure changes lead to a decreasing length-of-day in a warming climate. *Geophysical Research Letters*, *34*(6), 1–5. https://doi.org/10.1029/2006GL029106

Lenhart, H.-J., Mills, D. K., Baretta-Bekker, H., van Leeuwen, S. M., der Molen, J. V., Baretta, J. W., et al. (2010). Predicting the consequences of nutrient reduction on the eutrophication status of the North Sea. *Journal of Marine Systems*, *81*(1–2), 148–170. https://doi.org/10.1016/j.jmarsys.2009.12.014

Lentz, S., Guza, R., Elgar, S., Feddersen, F., & Herbers, T. (1999). Momentum balances on the North Carolina inner shelf. *Journal of Geophysical Research*, *104*(C8), 18205–18226. https://doi.org/10.1029/1999jc900101

Lin, W., Lin, H., Hu, J., & Huang, L. (2022). Relative contributions of open-ocean forcing and local wind to sea level variability along the west coasts of ocean basins. *Journal of Geophysical Research: Oceans*, *127*(11), e2022JC019218. https://doi.org/10.1029/2022jc019218

MacLachlan, C., Arribas, A., Peterson, K. A., Maidens, A., Fereday, D., Scaife, A. A., et al. (2015). Global seasonal forecast system version 5 (GloSea5): A high-resolution seasonal forecast system. *Quarterly Journal of the Royal Meteorological Society*, *141*(689), 1072–1084. https://doi.org/10.1002/qj.2396

Mangini, F., Chafik, L., Madonna, E., Li, C., Bertino, L., & Nilsen, J. E. Ø. (2021). The relationship between the eddy-driven jet stream and northern European sea level variability. *Tellus A: Dynamic Meteorology and Oceanography*, *73*(1), 1–15. https://doi.org/10.1080/16000870.2021.1886419

Marsh, R., Haigh, I. D., Cunningham, S. A., Inall, M. E., Porter, M., & Moat, B. I. (2017). Large-scale forcing of the European slope current and associated inflows to the North Sea. *Ocean Science*, *13*(2), 315–335. https://doi.org/10.5194/os-13-315-2017

Middleton, J. F., & Leth, O. K. (2004). Wind-forced setup of upwelling, geographical origins, and numerical models: The role of bottom drag. *Journal of Geophysical Research: Oceans*, *109*(12), 1–12. https://doi.org/10.1029/2003JC002126

Miller, L., & Douglas, B. C. (2007). Gyre-scale atmospheric pressure variations and their relation to 19th and 20th century sea level rise. *Geophysical Research Letters*, *34*(16), L16602. https://doi.org/10.1029/2007gl030862

O'Dea, E., Furner, R., Wakelin, S., Siddorn, J., While, J., Sykes, P., et al. (2017). The CO_5 configuration of the 7 km Atlantic Margin Model: Large-scale biases and sensitivity to forcing, physics options and vertical resolution. *Geoscientific Model Development*, *10*(8), 2947–2969. https://doi.org/10.5194/gmd-10-2947-2017

Permanent Service for Mean Sea Level. (2022). Tide gauge data [Dataset]. *Permanent Service for Mean Sea Level*. http://www.psmsl.org/data/obtaining/

Piecuch, C. G., Dangendorf, S., Gawarkiewicz, G. G., Little, C. M., Ponte, R. M., & Yang, J. (2019). How is New England coastal sea level related to the Atlantic meridional overturning circulation at 26°N? *Geophysical Research Letters*, *46*(10), 5351–5360. https://doi.org/10.1029/2019gl083073

Piecuch, C. G., Fukumori, I., Ponte, R. M., Schindelegger, M., Wang, O., & Zhao, M. (2022). Low-frequency dynamic ocean response to barometric-pressure loading. *Journal of Physical Oceanography*, *52*(11), 2627–2641. https://doi.org/10.1175/jpo-d-22-0090.1

Piecuch, C. G., & Ponte, R. M. (2015). Inverted barometer contributions to recent sea level changes along the northeast coast of North America. *Geophysical Research Letters*, *42*(14), 5918–5925. https://doi.org/10.1002/2015gl064580

Sturges, W., & Douglas, B. C. (2011). Wind effects on estimates of sea level rise. *Journal of Geophysical Research*, *116*(C6), C06008. https://doi.org/10.1029/2010jc006492

Thompson, P., & Mitchum, G. (2014). Coherent sea level variability on the North Atlantic western boundary. *Journal of Geophysical Research: Oceans*, *119*(9), 5676–5689. https://doi.org/10.1002/2014jc009999

Tinker, J., Palmer, M. D., Copsey, D., Howard, T., Lowe, J. A., & Hermans, T. H. (2020). Dynamical downscaling of unforced interannual sea-level variability in the North-West European shelf seas. *Climate Dynamics*, *55*(7–8), 2207–2236. https://doi.org/10.1007/s00382-020-05378-0

Tyler, R. H., & Sanderson, B. G. (1996). Wind-driven pressure and flow around an island. *Continental Shelf Research*, *16*(4), 469–488. https://doi.org/10.1016/0278-4343(95)00030-5

van Dorland, R., Beersma, J., Bessembinder, J., Bloemendaal, N., van den Brink, H., Brotons Blanes, H., et al. (2023). *Knmi national climate scenarios 2023 for The Netherlands* (Technical Report). Royal Netherlands Meteorological Institute, Ministry of Infrastructure and Water Management.

Vinogradova, N. T., Ponte, R. M., & Stammer, D. (2007). Relation between sea level and bottom pressure and the vertical dependence of oceanic variability. *Geophysical Research Letters*, *34*(3), L03608. https://doi.org/10.1029/2006gl028588

Vörösmarty, C. J., Fekete, B. M., Meybeck, M., & Lammers, R. B. (2000). Global system of rivers: Its role in organizing continental land mass and defining land-to-ocean linkages. *Global Biogeochemical Cycles*, *14*(2), 599–621. https://doi.org/10.1029/1999GB900092

Wakelin, S., Woodworth, P., Flather, R., & Williams, J. (2003). Sea-level dependence on the NAO over the NW European Continental Shelf. *Geophysical Research Letters*, *30*(7), 1403. https://doi.org/10.1029/2003gl017041

Wang, O., Lee, T., Piecuch, C. G., Fukumori, I., Fenty, I., Frederikse, T., et al. (2022). Local and remote forcing of interannual sea-level variability at Nantucket Island. *Journal of Geophysical Research: Oceans*, *127*(6), e2021JC018275. https://doi.org/10.1029/2021jc018275

Wise, A., Calafat, F. M., Hughes, C. W., Jevrejeva, S., Katsman, C. A., Oelsmann, J., et al. (2024). Data for "Using shelfedge transport composition and sensitivity experiments to understand processes driving sea level on the Northwest European Shelf" [Dataset]. *Zenodo*. https://doi.org/10.5281/zenodo.10627345

Wise, A., Harle, J., Bruciaferri, D., O'Dea, E., & Polton, J. (2021). The effect of vertical coordinates on the accuracy of a shelf sea model. *Ocean Modelling*, *170*, 101935. https://doi.org/10.1016/j.ocemod.2021.101935

Wise, A., Hughes, C. W., & Polton, J. A. (2018). Bathymetric influence on the coastal sea level response to ocean gyres at western boundaries. *Journal of Physical Oceanography*, *48*(12), 2949–2964. https://doi.org/10.1175/JPO-D-18-0007.1

Wise, A., Hughes, C. W., Polton, J. A., & Huthnance, J. M. (2020). Leaky slope waves and sea level: Unusual consequences of the beta effect along western boundaries with bottom topography and dissipation. *Journal of Physical Oceanography*, *50*(1), 217–237. https://doi.org/10.1175/jpo-d-19-0084.1

Wise, A., Polton, J. A., & Harle, J. (2024). Ocean model repository for "Using shelfedge transport composition and sensitivity experiments to understand processes driving sea level on the Northwest European Shelf" [Software]. *Zenodo*. https://doi.org/10.5281/zenodo.10665111

Wise, A., Polton, J. A., Hughes, C. W., & Huthnance, J. M. (2020). Idealised modelling of offshore-forced sea level hot spots and boundary waves along the North American East Coast. *Ocean Modelling*, *155*, 101706. https://doi.org/10.1016/j.ocemod.2020.101706

Woodworth, P., Maqueda, M. Á. M., Roussenov, V. M., Williams, R. G., & Hughes, C. W. (2014). Mean sea-level variability along the northeast American Atlantic coast and the roles of the wind and the overturning circulation. *Journal of Geophysical Research: Oceans*, *119*(12), 8916–8935. https://doi.org/10.1002/2014jc010520

Woodworth, P., Pouvreau, N., & Wöppelmann, G. (2010). The gyre-scale circulation of the North Atlantic and sea level at Brest. *Ocean Science*, *6*(1), 185–190. https://doi.org/10.5194/os-6-185-2010

Xu, F. H., & Oey, L. Y. (2011). The origin of along-shelf pressure gradient in the middle Atlantic bight. *Journal of Physical Oceanography*, *41*(9), 1720–1740. https://doi.org/10.1175/2011JPO4589.1

Young, E. F., & Holt, J. T. (2007). Prediction and analysis of long-term variability of temperature and salinity in the Irish Sea. *Journal of Geophysical Research*, *112*(C1), C01008. https://doi.org/10.1029/2005JC003386